2010

THE HUBBLE SPACE TELESCOPE WIDE FIELD CAMERA 3 EARLY RELEASE SCIENCE DATA: PANCHROMATIC FAINT OBJECT COUNTS FROM 0.2{2 MICRONS WAVELENGTH

R Windhorst

S Cohen

N Hathi

P McCarthy JR

R Ryan

See next page for additional authors

Submitted to the Astrophysical Journal Supplement Series, May, 2010
Preprint typeset using LaTeX style emulateapj v. 11/10/09

THE HUBBLE SPACE TELESCOPE WIDE FIELD CAMERA 3 EARLY RELEASE SCIENCE DATA: PANCHROMATIC FAINT OBJECT COUNTS FROM 0.2–2 MICRONS WAVELENGTH

Rogier A. Windhorst [1], Seth H. Cohen [1], Nimish P. Hathi [2], Patrick J. McCarthy [3], Russell E. Ryan, Jr. [4], Haojing Yan [5], Ivan K. Baldry [6], Simon P. Driver [7], Jay A. Frogel [8], David T. Hill [7], Lee S. Kelvin [7], Anton M. Koekemoer [9], Matt Mechtley [1], Robert W. O'Connell [10], Aaron S. G. Robotham [7], Michael J. Rutkowski [1], Mark Seibert [3], Richard J. Tuffs [11], Bruce Balick [12], Howard E. Bond [9], Howard Bushouse [9], Daniela Calzetti [13], Mark Crockett [14], Michael J. Disney [15], Michael A. Dopita [16], Donald N. B. Hall [17], Jon A. Holtzman [18], Sugata Kaviraj [14], Randy A. Kimble [19], John W. MacKenty [9], Max Mutchler [9], Francesco Paresce[20], Abihit Saha [21], Joseph I. Silk [14], John Trauger [22], Alistair R. Walker [23], Bradley C. Whitmore [9], & Erick Young [24]

Submitted to the Astrophysical Journal Supplement Series, May, 2010

ABSTRACT

We describe the Hubble Space Telescope (HST) Wide Field Camera 3 (WFC3) Early Release Science (ERS) observations in the Great Observatories Origins Deep Survey (GOODS) South field. The new WFC3 ERS data provide calibrated, drizzled mosaics in the mid-UV filters F225W, F275W, and F336W, as well as in the near-IR filters F098W (Y_s), F125W (J), and F160W (H) in 1–2 HST orbits per filter. Together with the existing HST Advanced Camera for Surveys (ACS) GOODS-South mosaics in the BVi'z' filters, these panchromatic 10-band ERS data cover 40–50 square arcmin from from 0.2-1.7 μm in wavelength at 0.″07–0.″15 FWHM resolution and 0.″090 multidrizzled pixels to depths of AB$\lesssim$26.0–27.0 mag (5-sigma) for point sources, and AB$\lesssim$25.5–26.5 mag for compact galaxies.

In this paper, we describe: a) the scientific rationale, and the data taking plus reduction procedures of the panchromatic 10-band ERS mosaics; b) the procedure of generating object catalogs across the 10 different ERS filters, and the specific star-galaxy separation techniques used; and c) the reliability and completeness of the object catalogs from the WFC3 ERS mosaics. The excellent 0.″07–0.″15 FWHM resolution of HST/WFC3 and ACS makes star-galaxy separation rather straightforward over a factor of 10 in wavelength to AB$\lesssim$25–26 mag from the UV to the near-IR, respectively. Our main scientific results are:

1) We present the resulting Galactic star counts and galaxy counts in 10 different filters. From the ERS data, these could be accurately determined from AB$\simeq$19 mag to AB$\lesssim$26 from the mid-UV to the near-IR, respectively.

2) Both the Galactic stars counts and the galaxy counts show mild but significant trends of decreasing count slopes from the mid–UV to the near-IR over a factor of 10 in wavelength.

3) We combine the 10-band ERS counts with the panchromatic GAMA counts at the bright end (10$\lesssim$AB$\lesssim$20 mag), and with the ultradeep BVizYJH HUDF counts and other available HST UV counts at the faint end (24$\lesssim$AB$\lesssim$30 mag). *The galaxy counts are now well measured over the entire magnitude range 10$\lesssim$ AB$\lesssim$ 30 mag from 0.2–2 μm in wavelength.*

4) We fit simple galaxy evolution models to these panchromatic galaxy counts over this entire flux range, using the best available 10-band local galaxy luminosity functions (LFs) from the GAMA survey, as well as simple prescriptions of luminosity and/or density evolution. *While these models can explain each of the 10-band counts from 10$\lesssim$ AB$\lesssim$ 30 mag well, no single one of these simple models can explain the counts over this entire flux range in all 10 filters simultaneously.*

5) The 10-band panchromatic ERS data base is very rich in structural information at all rest-frame wavelengths where young or older stars shine during the peak epoch in the cosmic star-formation rate (z$\simeq$1–2), and constitutes a unique new HST data base for the community to explore in the future.

Subject headings: galaxies: evolution — galaxies: counts — galaxies: luminosity function, mass function — infrared: galaxies — ultraviolet: galaxies

Rogier.Windhorst@asu.edu
[1] School of Earth and Space Exploration, Arizona State University, P.O. Box 871404, Tempe, AZ 85287
[2] Department of Physics & Astronomy, University of California, Riverside, CA 92521
[3] Observatories of the Carnegie Institution of Washington, Pasadena, CA 91101-1292

[4] Department of Physics, University of California, One Shields Avenue, Davis, CA 95616
[5] Center for Cosmology and AstroParticle Physics, The Ohio State University, Columbus, OH 43210
[6] Astrophysics Research Institute, Liverpool John Moores University, Birkenhead CH41 1LD, United Kingdom
[7] School of Physics and Astronomy, University of St Andrews, Fife KY16 9SS, UK
[8] Association of Universities for Research in Astronomy, Washington, DC 20005
[9] Space Telescope Science Institute, Baltimore, MD 21218
[10] Department of Astronomy, University of Virginia, Charlottesville, VA 22904-4325
[11] Max Planck Institute for Nuclear Physics (MPIK), Saupfercheckweg 1, D-69117 Heidelberg, Germany
[12] Department of Astronomy, University of Washington, Seattle, WA 98195-1580
[13] Department of Astronomy, University of Massachusetts, Amherst, MA 01003
[14] Department of Physics, University of Oxford, Oxford OX1 3PU, United Kingdom
[15] School of Physics and Astronomy, Cardiff University, Cardiff CF24 3AA, United Kingdom
[16] Research School of Astronomy & Astrophysics, The Australian National University, Weston Creek, ACT 2611, Australia
[17] Institute for Astronomy, University of Hawaii, Honolulu, HI 96822
[18] Department of Astronomy, New Mexico State University, Las Cruces, NM 88003
[19] NASA–Goddard Space Flight Center, Greenbelt, MD 20771
[20] INAF–IASF Bologna, Via Gobetti 101, 40129 Bologna, Italy
[21] National Optical Astronomy Observatories, Tucson, AZ 85726-6732
[22] NASA–Jet Propulsion Laboratory, Pasadena, CA 91109
[23] Cerro Tololo Inter-American Observatory, La Serena, Chile
[24] NASA–Ames Research Center, Moffett Field, CA 94035

1. INTRODUCTION

1.1. *Scientific Background*

The study of the formation and evolution of galaxies and large scale structure are amongst the most active interfaces between theory and observation in modern astrophysics. Galaxies are believed to have formed gradually over cosmic time from a combination of merging and internal star-formation (Hopkins et al. 2006), regulated by feedback from stellar winds, supernovae, and/or AGN (Scannapieco et al. 2005; di Matteo, Springel, & Hernquist 2005). The origin of the Hubble sequence is not yet understood, but is likely related to the balance between major mergers versus minor accretion events and steady infall (Conselice 2003; Hopkins et al. 2010) The critical epoch for the assembly of massive galaxies appears to be the ∼4 Gyr span from redshift z≃3 to z≃1 (*e.g.*, Driver et al. 1998).

At redshifts $\gtrsim$2–3, deep Hubble Space Telescope (HST) imaging surveys and ground-based spectroscopy have revealed a paucity of massive galaxies and few classical disks or spheroids (Law, 2007, 2009). In contrast, large ground-based spectroscopic surveys targeting z$\lesssim$1 — coupled with HST imaging — have shown that by this epoch massive galaxies are largely mature, and that the Hubble sequence is well developed (*e.g.*, Abraham et al. 1995, 2007; Driver et al. 1998; Lilly et al. 1998). While there may be about a ∼50% growth in the stellar mass in spheroids in the last ∼7 Gyr, the process of major galaxy assembly was largely completed by z≃1 (*e.g.*, de Lucia et al. 2006; Dickinson et al.2003). The interim period — from redshifts of z∼3 to z∼1 — is the era in which most of the stellar mass in galaxies is accumulated (Dickinson et al. 2003), and when galaxies acquire the characteristic structural and dynamical properties that define them today. The HST Wide Field Camera 3 (WFC3) was designed and built to study this critical epoch of galaxy assembly in detail. This has become one of the driving reasons of the ERS project.

1.2. *Science Aspects of the WFC3 ERS program*

WFC3 was successfully installed into HST on May 14, 2009, by the astronauts on-board Space Shuttle Discovery during the Space Transportation System mission 125 (STS-125). This shuttle mission was the fifth Servicing Mission of HST, for historical reasons referred to as SM4. Many of the current co-authors were members of the WFC3 Science Oversight Committee (SOC) from July 1998 through November 2009. Our main role as SOC was to define the WFC3 science requirements and goals, monitor them during the pre-launch phases of the project, and to oversee the design, implementation, integration, plus ground-based and on-orbit testing of the WFC3 instrument.

The WFC3 was designed to provide a unique opportunity to make the connection between the galaxy populations in the local and distant universe, amongst many of its possible science goals. With the exquisite spectral coverage (0.2–1.7 μm), very high spatial resolution (0.″04–0.″16 FWHM), fine pixel sampling (0.″039–0.″13 FWHM), and high sensitivity of WFC3 (AB$\lesssim$26–27 mag in 2 orbits; 10-σ for point sources), many new interesting questions and outstanding problems can be addressed with the WFC3 ERS data. By sampling the vacuum UV with high sensitivity and the very high angular resolution afforded by the diffraction limited 2.4 m Hubble Space Telescope, WFC3 can observe star-forming regions in galaxies over most of the Hubble time. The near-IR channel on WFC3 allows one to do restframe visible band photometry of distant galaxies to very low stellar masses, and over areas large enough to provide representative samples. Together, the panchromatic images produced by WFC3 allows the user to decompose distant galaxies into their constituent substructures, examine their internal stellar populations, and help constrain their dust content. In this early release science program, the UVIS and IR channels of WFC3 are used to provide a small, but representative sampling of the capabilities of WFC3 to examine the formation and evolution of galaxies in the critical galaxy assembly epoch of z≃1–3, when the universe was only 6–2 Gyrs old, respectively.

The high spatial resolution panchromatic WFC3 ERS data set allows the user to gauge the growth of galaxies through star-formation and merging. High precision photometric and low-resolution spectroscopic grism redshifts allow one to make accurate determinations of the faint-end of the galaxy luminosity and mass functions, and helps shed light on merging and tidal disruption of stellar and gaseous disks. The WFC3 images also allow one to make detailed studies of the internal structure of galaxies, and the distribution of young and old stellar populations. This program demonstrates the unique power of WFC3, by applying its many diverse modes and full panchromatic capability to forefront problems in astrophysics. Details of HST ERS program (PID #11359; PI R. O'Connell) can be found on this URL[25]. The current ERS program was specifically conceived to make maximum use of the WFC3 capabilities — while the instrument was designed and constructed made from 1998–2008 — and to allow for optimal comparison of the intermediate and high redshift galaxy samples identified in the current ERS program to nearby galaxy HST programs.

In §2 of this paper, we present the WFC3 ERS survey strategy, the ERS filters used and their achieved depths. In §3, we present the ERS observations in both the WFC3 UVIS and IR channels, and the ERS pointings and their areal coverage. In §4, we present the WFC3 ERS data reduction procedures and their reliability and current limitations. In §5, we present the ERS object finding procedures and catalog generation, and the star-galaxy

[25] http://www.stsci.edu/cgi-bin/get-proposal-info

separation procedure used in the 10 ERS filters. In §6, we present the panchromatic ERS star counts and galaxy counts from 0.2–1.7 μm to AB$\lesssim$26-27 mag, and compare these to the 10-band ground-based GAMA counts from 10$\lesssim$AB$\lesssim$20 mag at the bright end, and the HUDF counts in BVizYJH filters from 24$\lesssim$AB$\lesssim$30 mag at the faint end. We also present the panchromatic ERS images of interesting individual objects. In §7, we summarize our main results and conclusions. Throughout this paper, we use WMAP-year7 cosmology (Komatsu et al. 2010), or H_0 =71 $km\ s^{-1}\ Mpc^{-1}$, Ω_o=0.26, and Λ=0.74.

2. WFC3 AND ITS CAPABILITIES

2.1. *The ERS Filter Set*

In the current ERS program, the unique panchromatic capabilities of WFC3 are used to survey the structure and evolution of galaxies at the peak of the galaxy assembly epoch at z$\simeq$1–3. Deep ultraviolet and near-IR imaging, and slitless near-IR spectroscopy of existing deep multi-color GOODS/ACS fields are used to gauge star-formation and the growth of stellar mass as a function of galaxy morphology, structure and surrounding density in the critical cosmic epoch at redshifts 1$\lesssim$z$\lesssim$3.

The total HST filter set provided by the WFC3 ERS imaging of the GOODS fields is shown in Fig. 1a. WFC3 adds the F225W, F275W and F336W filters in the WFC3 UVIS channel, and the F098M, F125W and F160W filters in the WFC3 IR channel. Together with the existing GOODS ACS F435W, F606W, F775W and F850LP images, the new WFC3 UVIS and IR filters provide a total of 10 HST filters that span the wavelength range $\lambda\simeq$0.2–1.7 μm nearly contiguously. We refer to this entire survey — including the new WFC3 data and the existing GOODS-S ACS v2.0 data in BViz — hereafter as the "ERS". Details of the GOODS survey can be found in Giavalisco et al. (2004) and references therein. Fig. 1a compares the ERS filters to the spectral energy distribution of model galaxies at z$\simeq$1.0, 1.5 and 2.5 with ages of 3, 2 and 1 Gyr, respectively. Fig. 1a illustrates that the WFC3 UV filters are particularly powerful in accessing the Lyman-α forest and Lyman continuum breaks at redshifts z$\simeq$1–3.

The ERS images in the WFC3 UVIS filters F225W, F275W, and F336W are used to identify galaxies at z$\lesssim$1.5 from their UV continuum breaks, and provide star-formation indicators tied directly to both local and z$\gtrsim$3 galaxy populations, which are the ones best observed through their Lyman breaks from the ground at $\lambda\gtrsim$350 nm. The critical new data that the WFC3 UVIS channel can provide are thus very high resolution, deep vacuum mid-UV images from 0.2$\lesssim\lambda\lesssim$0.3 μm.

The ERS images in the WFC3 near-IR filters F098M, F125W and F160W are used to probe the Balmer and 4000 Å breaks and stellar mass function well below 10^9 $M_\odot$ for mass-complete samples in the redshift range z$\simeq$1–3. The unique new data that the WFC3 UVIS channel can provide are high resolution, very sensitive near-IR photometry over fields larger than those possible with HST NICMOS, or with adaptive optics from the ground (*e.g.*, Steinbring et al. 2004; Melbourne et al. 2005).

2.2. *ERS Grisms Used*

In addition to these broad-band filters, we used the WFC3 near-IR grisms G102 and G141 to obtain slitless spectroscopy of hundreds of faint galaxies at a spectral resolution of R$\sim$130–210. The WFC3 near-IR grism data can trace the primary indicators of star-formation — the Lyman-α and H-α emission-lines — in principle over the redshift range from z$\simeq$5–13 and z$\simeq$0.2–1.7, respectively. WFC3 can also trace the Lyman plus the rest-frame UV continuum slope, as well as the Balmer plus 4000 Å-breaks over the redshift range z$\simeq$1–9 and z$\simeq$0–2.5, respectively. The ERS grism program thus at least covers the peak of the cosmic star formation history at redshifts 1$\lesssim$z$\lesssim$2, using some of the most important star-formation and post-starburst indicators, while also providing some metallicity-independent reddening indicators. Both IR grism dispersers provide capabilities, that cannot be reproduced from the ground: slitless spectroscopy of very faint objects (AB$\lesssim$25–26 mag) over a contiguous wide spectral range in the near-IR, that is not affected by night-sky lines.

The addition of the low-resolution (R $\simeq$ 130–210) near-IR spectra also allows the user to obtain accurate spectro-photometric redshifts for objects as faint as AB$\simeq$25 mag (*cf.* Pirzkal et al. 2004; Malhotra et al. 2005, Straughn et al. 2008, 2009, Cohen et al. 2010). The redshift precision is expected to be a few percent or $\sigma_z/(1+z)\lesssim$0.04 (Ryan et al. 2007), allowing accurate determination of the faint-end of the galaxy luminosity function (LF), and to find potential fainter members of known small-scale galaxy clustering and large-scale structures in the redshift range z$\simeq$0.5–3 across the WFC3 ERS mosaics. Such grism data cannot provide precise spectroscopic redshift measurements to identify true large scale structure, but it allows one to do statistical studies of spatially close objects with similar spectro-photometric redshifts, that have a high likelihood to be at similar distances, which *e.g.*, helps determine the epoch-dependent galaxy major merger rate (Ryan et al. 2008). Details of the ERS grism data reduction and its analysis are given by Straughn et al. (2010) and Kuntschner et al. (2010).

WFC3 UVIS G280 UV-prism observations were not done as part of the ERS, because of its much lower throughput and the significant overlap of its spectral orders (Bond & Kim Quijano 2007; Wong et al. 2010).

2.3. *WFC3 Detectors and Achieved ERS Sensitivities*

The very sensitive ERS observations were made possible by assuring that the WFC3 had the best possible CCD and near-IR detectors. WFC3s UV—blue optimized CCDs were chosen specifically to complement those of ACS. They were made by E2V in the UK, and are thinned, backside illuminated, CCD detectors with 2k×4k 15 μm (0.″0395) pixels, covering the wavelength range 200–1000 nm with QE$\gtrsim$50% throughout (Wong et al. 2010).

The WFC3 near-IR detectors were Teledyne HgCdTe infrared detectors, and were MBE-grown, substrate removed, with Si CMOS Hawaii-1R multiplexers, and have 1k×1k 18 μm (0.″130) pixels, covering the wavelength range 800–1730 nm with QE$\gtrsim$77% throughout (Wong et al. 2010). Further specifications of the WFC3 detectors are listed where relevant below.

Table 1 summarizes the resulting excellent WFC3 sensitivities from our relatively short ERS exposures. The table lists the number of orbits per filter and the 5-σ depths in AB magnitudes and F_ν units. A net exposure time of 2600–2700 seconds was available in each HST orbit for on-source ERS observations. In Fig. 1b, the equivalent depths are plotted in physical terms, by comparing with with spectral synthesis models of Bruzual & Charlot (2003) at the three fiducial redshifts, following Ryan et al. (2007, 2010). Simple stellar populations models are plotted with single bursts, or exponentially declining star-formation rates with an e-folding time of 1 Gyr. Fig. 2b shows the predicted spectral energy distributions for models with ages ranging from 10 Myr to 3 Gyr, along with the 5-σ depths of the WFC3 ERS program. The three panels represent redshifts z=1.0, 1.5 and 2.0, and models with stellar masses of M=10^9, 4×10^9, and 10^{10} $M_\odot$, respectively. These SED tracks illustrate the intended SED and mass sensitivity of the WFC3 ERS observations as a function of cosmic epoch. Galaxies with ongoing star-formation, even with fairly large ages, are easily detected in the WFC3 mid-UV observations. At z$\simeq$2, a maximally old $\tau\simeq1$ model with a mass of $\sim$0.3 M* is detectable above the WFC3 detection threshold in the F336W filter, while at z$\simeq$1, the WFC3 ERS can detect young star forming galaxies with masses as low as a few$\times10^7$ $M_\odot$, or about a M$\sim$0.01 M* galaxy in that filter.

Table 2 summarizes the high level parameters of the HST instrument modes, the ERS filters used, the filter central wavelength λ, its width $\Delta\lambda$ or FWHM — both in μm — the PSF FWHM as a function of wavelength, the zero-points for all 10 ERS filters in units of $1.0e^-$ /sec, as well as the zodiacal sky-background measured in each ERS filter. The GOODS BViz sky-background values are from Hathi et al. (2008).

Fig. 2 shows that on average, the on-orbit WFC3 UVIS sensitivity is 6–18% higher than the predicted pre-launch sensitivity from the ground-based thermal vacuum test (left panel), and the on-orbit WFC3 UVIS sensitivity is 9–18% higher (right panel). This beneficial, but significant discrepancy is believed to result from uncertainties in the absolute calibration procedure of the optical stimulus used in the Thermal Vacuum tests of WFC3. The cause of this 6–18% discrepancy is currently being investigated, and lessons learned will be applied to the upcoming ground-based calibrations of the James Webb Space Telescope Thermal Vacuum absolute throughput measurements.

3. THE ERS DATA COLLECTION STRATEGY

3.1. *ERS Pointings and Areal Coverage*

To make the best use of the limited HST spacecraft time, the WFC3 ERS program is most efficiently carried out in existing HST Treasury fields. The two Great Observatories Origin Deep Survey (GOODS) fields are among the best candidate fields. They contain deep four-color ACS imaging (Giavalisco et al. 2004; Dickinson et al. 2004), and ACS slitless G800L grism spectra covering wavelengths from $\sim$0.55–0.95 μm (*cf.* Pirzkal et al. 2004; Malhotra et al. 2005, Straughn et al. 2008, 2009). There is also a wealth of ground- and space-based data, such as deep VLT K-band imaging (Labbé et al. 2003), a large number of VLT spectra (Vanzella et al. 2006), deep Chandra X-ray images (Giacconi et al. 2002), Spitzer photometry with IRAC and MIPS (Dickinson et al. 2006; Yan et al. 2004, 2005), and deep VLA and ATCA radio images (*cf.* Afonso et al. 2006, Kellermann et al. 2008).

3.2. *ERS Mosaics and WFC3 Scheduling*

Given the constraint on the total amount of time available — and the desire to use the above WFC3 panchromatic filter set — in the allotted HST time of 104 orbits, the ERS program could survey one 4×2 WFC3 mosaic covering 10′ ×5′ or roughly 50 arcmin^2 to 5-sigma depths of $m_{AB} \simeq 26.0$ mag in the three bluest wide-band UVIS filters, and one 5×2 WFC3 mosaic covering 10′ ×4′ or roughly 40 arcmin^2 to 5-sigma depths of $m_{AB} \simeq 27.0$ mag in the three near-IR filters. These angular scales probe comoving scales of roughly 5–10 Mpc, and provides a sample of 2000–7000 galaxies to AB$\lesssim$26–27 mag in the panchromatic ERS images. The IR images were dithered to maximally match the UVIS field of view. The layout of these ERS UVIS and IR mosaics is given in Fig. 3, compared to the other ACS data that are available in the GOODS-South field, as well as the ACS images taken in parallel to the ERS data.

Fig. 3 shows the ACS z'-band (F850LP) mosaic of the entire GOODS-South field, and the outline of the acquired WFC3 pointings, as well as the locations of some of the other ACS data sets. The WFC3 ERS mosaic pointings cover the Northern $\sim$30% of the GOODS-South field (Fig. 3). The 8 ERS pointings are contiguous, with a tiling that can be easily extended to the South in future WFC3 GO programs.

HST scheduling required that this ERS program be split into several visits. Simple raster patterns were be used to fill out the WFC3 IR mosaic, and to improve sky plus residual dark-current removal. Only mild constraints were applied to the original HST roll angle (ORIENTs) to maximize overlap between the northern part of the GOODS-South field, and to allow HST scheduling in the permitted observing interval for the ERS (mid-Sept.–mid-Oct. 2009). The IR and UVIS images were constrained to have the *same* ORIENT, to ensure that a uniform WFC3 mosaic could be produced at all wavelengths. The slight misalignment of the Northern edge of the *existing* ACS GOODS-South mosaics and the *new* WFC3 ERS mosaics in Fig. 3 was due to the fact that the HST ORIENT constraints had changed in the late summer of 2009, because the ERS observations were postponed by several weeks due to a change in the HST scheduling constraints.

The area of overlap between the individual WFC ERS mosaic pointings is too small to identify transient objects (e.g. SNe and variable AGN), since only about 1–2% of all faint field objects show point-source variability (Cohen et al. 2006). However, it is useful in the subsequent analysis to verify the positions of objects, and so verify the instrument geometrical distortion corrections (GDCs) used, as discussed in §4 and Appendix A.

4. WFC3 UVIS AND IR DATA PROCESSING

The WFC3 ERS data processing was carried out with the STScI pipeline calwf3. The WFC3 ERS data set also provided tests of the STSDAS pipeline under realistic conditions. This process was started well before the SM4 launch in the summer of 2008 with pre-flight WFC3 thermal vacuum calibration data, and continued through the late summer and fall of 2009, when the first ERS data arrived. The raw WFC3 data was made public immediately, and the OTF pipe-lined and drizzled WFC3 mosaics will be made public via MAST at STScI when the final flight calibrations — as detailed below — have been applied. The specific pipeline corrections that were applied to the WFC3 ERS images are detailed here. Unless otherwise noted below, the latest reference files from the WFC3 Calibration web-page were used in all cases, and are on this *URL*[26]

4.1. *The Main WFC3 Pipeline Corrections*

4.1.1. *WFC3 UVIS Pipeline Corrections*

All raw WFC3 UVIS data were run through the standard *STSDAS calwf3* pipeline as following:

(1) The current best available WFC3 UVIS super-bias (090611120_bia.fits) was subtracted from all images. This is an on-orbit super-bias created from 120 UVIS bias frames, each of which was unbinned, and used all four on-chip amplifiers (see *URL*[27]. The measured on-orbit UVIS read-noise levels are $3.1e^-$ in Amp A, $3.2e^-$ in Amp B, $3.1e^-$ in Amp C, and 3.2 e^- in Amp D, respectively, or on average about 3.15 e^- per pixel across the entire UVIS array.

(2) A null dark frame was applied, since the only available darks at the time were from the ground-based thermal vacuum testing in 2007–2008, and were not found to reduce the noise in the output ERS frames. Hence, the subtraction of actual on-orbit 2D dark-frames was omitted until better, high signal-to-noise ratio on-orbit dark-frames have been accumulated in Cycle 17 and beyond. Instead, a *constant* dark-level of 1.5 e^- /pix/hr was subtracted from all the images, as measured from the *average* dark-current level in the few on-orbit dark-frames available thus far. This dark-level is about 5× higher than the ground-based thermal vacuum tests had suggested, but still quite low enough to not add significant image noise in an average 1300 sec UVIS exposure.

(3) A bad pixel file (tb41828mi_bpx.fits) was created (by H. Bushouse) and updated over the one available in OPUS at the time, and applied to all the UVIS images.

(4) All flat-fields came from the 2007–2008 WFC3 thermal vacuum ground tests, and had high signal-to-noise ratio, but left some large-scale gradients in the flat-fielded data, due to the illumination difference between the thermal vacuum optical stimulus and the real on-orbit WFC3 illumination by the zodiacal sky. For each passband, the mean UV-sky was removed from the individual ERS images, and the resulting images were combined into a median image in each UV filter. The large scale gradients from this illumination difference correspond to a level of about ∼5–10% of the on-orbit zodiacal sky background, and have very low spatial frequency. This situation will be remedied with on-orbital internal flats and sky-flats, that will be accumulated during the course of Cycle 17 and beyond. Since the UV sky is very low to begin with (∼25.46 mag arcsec^{-2} in F225W, 25.64 mag arcsec^{-2} in F275W, and 24.82 mag arcsec^{-2} in F336; see Table 2 here and also Windhorst et al. 2002), these residual $\lesssim$5–10% sky-gradients affect the object photometry only at the level of AB$\gtrsim$27–28 mag, *i.e.*, well below the catalog completeness limits discussed in §4, and hence does not significantly impact the construction of complete samples from our UVIS images to AB$\lesssim$25.5–26.0 mag.

We suspect, but have at this stage not been able to prove with the currently available data, that this remaining low-level sky gradient is of *multiplicative* and not of *additive* nature. Once we have been able to demonstrate this with the full suite of Cycle 17 sky-flats, we will re-process all the UVIS data again, and remove these low-level gradients accordingly. For now, they are not visible in the high quality, high contrast color reproductions of

[26] www.stsci.edu/hst/observatory/cdbs/SIfileInfo/WFC3/reftablecurrentdir
[27] http://www.stsci.edu/hst/wfc3/new_uvis_bias_lbn

Figs. 4–5. Hence, they do not significantly affect the subsequent object-finding and their surrounding sky-subtraction procedures (to AB$\lesssim$25.5–26.0 mag), which assume linear remaining sky-gradients. This is corroborated by the quality of the panchromatic object counts discussed below, and its consistency with the counts from other authors at the flux range of overlap. In other words, any remaining low-level sky gradients do not significantly affect the object catalogs generated for the current science purposes to AB$\lesssim$25.5–26.0 mag.

4.1.2. *WFC3 IR Pipeline Corrections*

The reduction of the ERS WFC3 IR data largely followed the procedures as described in Yan et al. (2009). We used the calwf3 task included in the STSDAS package to process the raw WFC3 IR images, using the latest reference files indicated by the relevant FITS header keywords:

(1) We removed the artificial quadrature "pedestal" signature (caused by the IR gain being corrected twice in the current calwf3 pipeline version), using the average gain value — $< g >$=1.54 over that of the four amplifiers, which ranges from g_i=1.52–1.56 — as given in the WFC3 STAN (September 2009 issue; see URL[28]; see also Wong et al. 2010). Specifically, after correcting for the fact that g=1.54 was applied twice, the incremental multiplicative gain values applied (once) were 1.004 for Quadrant 1 (upper left), g = 0.992 for Quadrant 2 (lower left) = 0.992, g=1.017 for Quadrant 3 (lower right), and g=0.987 for Quadrant 4 (upper right quadrant).

(2) For each passband, the mean near-IR sky was removed from the individual ERS images, and the resulting images were combined into a median image in each near-IR filter.

(3) A smooth background gradient still persisted in the median image. This gradient was fitted by a 5-order Spline-3 function, and was then subtracted from the individual near-IR images. This sky gradient is of order 1–2% of the zodiacal sky-background. Since the near-IR zodiacal sky background is about 22.61, 22.53, and 22.30 mag arcsec^{-2} in Y_sJH, respectively. (see Table 2), these remaining WFC3 IR gradients do not affect the large-scale object finding and catalog generation at levels brighter than AB$\simeq$27.0 mag.

4.2. *WFC3 Astrometry and Multidrizzle Procedures*

4.2.1. *WFC3 UVIS Astrometry*

The calibrated, flat-fielded WFC3 UVIS exposures were aligned to achieve astrometric registration with the existing GOODS ACS reference frame (Giavalisco et al. 2004; GOODS v2.0 from Grogin et al. 2009). To generate accurate SExtractor (Bertin & Arnouts 1996) object catalogs in the F225W, F275W and F336W filters, the higher S/N-ratio GOODS ACS B-band images were used as the detection image. This also provided an astrometric reference frame that was matched as closely as possible to the wavelengths of the UVIS filters used in these observations. Because the GOODS B-band images reach AB$\gtrsim$28.0 mag and so go much deeper than the ERS UVIS images, they help optimally locate the objects in the ERS UVIS mosaics.

Furthermore, the orbital F225W and F275W ERS observations were designed to minimize possible Earth limb contamination. To guarantee the lowest possible UV sky in the WFC3 images, only one exposure was obtained in F225W at the end of each orbit, in contrast with the common practice of observing all exposures in the same filter in rapid succession in subsequent orbits. (All three F336W exposures were obtained during the same single orbit for a given ERS pointing). This manner of scheduling indeed minimized the on-orbit UV sky away from the Earth's limb (see Table 2), but somewhat complicated the sub-sequent multidrizzle procedure, since no "same-orbit" cosmic ray rejection could be applied in F225W and F275W, to allow one to find a first slate of bright objects for image alignment.

As a result, the F225W and F275W ERS exposures taken in successive orbits needed to be aligned with each other individually, in addition to their overall alignment onto the GOODS reference frame. For each ERS filter, the relative alignment between exposures was achieved iteratively, starting with an initial partial run of multidrizzle (Koekemoer et al. 2002) to place each exposure onto a rectified pixel grid. These images were then cross-correlated with each other, after median-filtering a smoothed version of each UVIS exposure to reduce the impact of cosmic rays and to identify the brighter real objects. This ensured a relative alignment between the sequential orbital ERS exposures to the subpixel level, correcting offsets that were introduced by the guide-star acquisitions and re-acquisitions at the start of each successive orbit.

4.2.2. *The WFC3 UVIS Multidrizzle Procedure*

These first-pass aligned images were then run through a full combination with multidrizzle (Koekemoer 2002), which produced a mask of cosmic rays for each exposure, together with a cleaned image of the field. The cosmic ray mask was used to create a cleaner version of each exposure, by substituting pixels from the clean, combined image. These were then re-run through the cross-correlation routine to refine the relative shifts between the exposures, achieving an ultimate relative alignment between exposures of $\lesssim$2–5 mas. This process was limited primarily by the on-orbit cosmic ray density, and the available flux in the faint UV objects visible in each individual UVIS exposure. In the end, about 3 independent input pixels from 4 exposures contributed to *one* multidrizzle UVIS output pixel. Of these, typically $\lesssim$1–2% were re-

[28] http://www.stsci.edu/hst/wfc3/STAN_09_2009

jected in the cosmic ray rejection, leaving typically 3 independent UVIS measurements contributing to one multidrizzle output pixel in both the F225W and F275W filters. In F336W, about 2.3 independent input pixels from the 3 F336W exposures contributed to one output pixel during the multidrizzle process.

After this relative alignment between exposures was successfully achieved, each set of exposures needed to be aligned to the *absolute* GOODS astrometric reference frame. This was achieved by generating catalogs from the cleaned, combined images for each of the three ERS UVIS filters F225W, F275W, and F336W, and matching them to the GOODS B-band catalog (Giavalisco et al. 2004; Grogin et al. 2009). This was done by solving for linear terms (shifts and rotations) using typically ∼30–50 objects matched in each pointing, depending on the UVIS filter used. This procedure successfully removed the mean shift *and* rotational offsets for each visit relative to the GOODS astrometric frame. Multidrizzle also produced "rms-" or "weight"-maps (Koekemoer 2003), which are essential for the subsequent object detection (§5.1), and for the computation of the effective area, which is needed for the object counts (see the figures in §6).

In order to perform matched aperture photometry (see §5.2), our approach was to create images at *all* wavelengths at the same pixel-scale. Since the IR data was necessarily created at 0.″090 per pixel (see Appendix A), we created UVIS mosaics at that same pixel size. This essentially "smoothed" over the remaining issue of the geometrical distortion solution (see Appendix A), and created a sufficient data product for the purpose of producing matched aperture photometric catalogs, reliable total magnitudes in all 10 ERS filters, performing z≃1–3 dropout searches, and many other "total magnitude applications". The performance of the panchromatic ERS images for photometric redshift estimates is described by Cohen et al. (2010). Further details on the remaining uncertainties from the UV geometrical distortion and its corrections are given in Appendix A and Fig. 4a–4b.

The current 0.″090 per pixel UVIS image mosaic is referred to as "ERS version v0.7". In the future, when the UV geometrical distortion correction is well measured and more dither points for the ERS UV images are available, we will make higher resolution images (0.″030 per pixel) for applications such as high-resolution faint-galaxy morphology, structure, half-light radii, and other high-precision small-scale measurements of faint galaxies, and make these end-products available to the community.

4.2.3. *IR Astrometry and Multidrizzle Procedure*

The WFC3 IR images processed in section 3.1 were first corrected for the instrument geometric distortion, and then projected to a pre-specified astrometric reference grid according to the WCS information populated in the image headers. This was done by using the multidrizzle software (Koekemoer et al. 2002) distributed in the STSDAS.DITHER package. Similar to the processing of the UVIS images in §4.2.1, the GOODS version 2.0 ACS mosaics were used as the astrometric reference. The only difference is that the GOODS ACS mosaics were straightly 3×3 rebinned for comparison with the ERS IR data, giving a spatial resolution of 0.″090 per pixel for all ERS images.

As usual, the projected ERS IR images show non-negligible positional offsets, which is mainly caused by the intrinsic astrometric inaccuracies of the guide stars used in the different HST visits. Following Yan et al. (2009), about 6–12 common objects were were manually identified in each ERS IR input image and in the reference ACS z_{850} image, and we subsequently solved for X-Y shift, rotation, and plate scale between the two. These transformations were then input to multidrizzle, and the drizzling process was re-run to put each input image onto the pre-specified grid. We set the drizzling scale ("pixfrac") to 0.8, so that in the IR, about 5 input pixels from 6 exposures, or 20 independent measurements contributed to one multidrizzle output pixel. Of these, typically $\lesssim$10% or 2 pixels were rejected in the cosmic ray rejection, leaving typically 18 independent measurements contributing to one multidrizzle output pixel.

4.3. *Resulting ERS Mosaics and their Properties*

4.3.1. *The panchromatic 10-band ERS mosaics*

Fig. 5a. shows the panchromatic 10-band color image of the entire ERS mosaic in the CDF-South. All RGB color images of the 10-band ERS data were made as following. First, the mosaics in all 10 filters have the common WCS of the ACS GOODS v2.0 reference frame to well within one pixel. Second, all images were rescaled to F_ν units of Jy per pixel using the AB zero-points of Table 2. Next, the blue gun of the RGB images contained a weighted version of the UVIS images in the F225W, F275W, and F336W filters and the ACS F435W filter. The green gun contained a weighted version of the ACS F606W and F775W images, which had the highest S/N-ratio of all available images. The red gun contained a weighted version of the ACS z-band (F850LP) and WFC3 IR F098M, F125W, and F160W images. All weighting was done with the typical image sky S/N-ratio, sometimes adjusted so as to not overemphasize the deepest multi-epoch GOODS v2.0 images in the V and i-filters. This procedure thus also rebalanced the different sensitivities per unit time in these filters, as shown in Fig. 1a–1b, and corrected for the fact that some filters overlap somewhat more than at the usual FWHM wavelength values (see Table 1). This is especially noticeable for the ACS z-band filter F850LP — which at the long wavelength side is cut-off by the sharp decline in the QE-curve of silicon — and the IR F098M filter, which doesn't have this problem at its blue side, but over-

laps with F850LP for about 40% of its OTA×QE×T integral. (When the QE of the HgCdTe detectors produced by Teledyne increased from ∼10–20% in 2001 to ≳80% after 2005, the F098M filter became thus almost a replacement of the ACS z-band.

In Fig 5a–5b, we used log(log) stretch to optimally display the enormous dynamic range of the full resolution ERS color TIFF images. Fig. 5a only displays the part of the common cross sections between the 4×2 ERS UVIS mosaics, the GOODS v2.0 ACS BViz, and the 5×2 ERS IR mosaics. Each of the ERS mosaics are 8079 × 5540 pixels in total, but only about 6500 × 3000 pixels or 9.75 × 4.5 or 43.875 arcmin^2 is in common between the UVIS and IR mosaics, and shown in Fig. 5a–5b. The area of the individual UVIS mosaics that is used in each of the UV-optical galaxy counts of §6 is substantially larger than this, but the total usable area of the IR mosaics is comparable to the area shows in Fig. 5a.

Fig. 5b shows a zoom of the 10-band ERS color image in the CDF-South, illustrating the high resolution available over a factor of ten in wavelength, the very large dynamic range in color, and the significant sensitivity of these few orbit panchromatic ERS images. Further noteworthy objects in the ERS images are discussed in §6.5 below.

4.3.2. *The panchromatic ERS PSFs*

Fig. 6a shows a full color reproduction of a stellar image in the 10-band ERS color images in the CDF-South, and Fig. 6b shows a double star. These images give a qualitative impression of the significant dynamic range in both intensity and wavelength that is present in the ERS images. Fig. 7a show images in all 10 ERS filters of an isolated bright star that was unsaturated in all filters, and Fig. 7b shows its 10-band stellar light-profiles. Table 2 shows the stellar PSF FWHM values in the 10 ERS bands. These include the contribution form the OTA and its wavefront errors, the specific instrument pixel sampling or Modulation Transfer Function (MTF).

Table 2 and Fig. 7b show the progression of the HST λ/D values with wavelength in the 10 ERS filters. Table 2 implies that the larger pixel values used in the multidrizzling of §4.1.2 indeed add to the effective PSF diameter. Table 2 also shows that that HST is diffraction limited in V-band and longwards, while shortward of V-band, the PSF FWHM starts to increase again due to mirror micro-roughness in the ultraviolet. At wavelengths shorter than the V-band, HST is no longer diffraction limited, resulting in wider image-wings, and a somewhat larger fraction of the stellar flux visible outside the PSF-core. The "red halo" at $\lambda \gtrsim 0.8$ μm is due to noticeable Airy rings in the stellar images in the WFC3 IR channel, and the well known red halo in the ACS z-band (Maybhate et al. 2010) has an additional component due to light scattered off the CCD substrate.

4.3.3. *The 10-band ERS Area and Depth*

Table 1 summarizes the exposure times and the actual achieved depth in each of the observed ERS filters, while Table 2 also lists the effective area covered in each filter mosaic at the quoted depth.

The histograms of Fig. 8a give the cumulative distribution of the maximum pixel area that possesses a specified fraction of total orbital exposure time. These effective areas must be quantified in order to properly do the object counts in Fig. 11. After Multi-drizzling the ERS mosaics in the UV and IR, these effective areas were computed from the weight maps, which include the total exposure time, and the effects from CR-rejection, dithering, and drizzling. Fig 8a shows that about 50 arcmin^2 of the UV mosaics has ∼80% of the UVIS exposure time or ∼90% of the intended UV sensitivity. For reference, one $''.09$ pixel could be composed of 5.2 native WFC3 UVIS pixels times the number of exposures on that portion of sky. Due to overlapping dithers (see Fig. 3), some pixels have more than the total orbital exposure time contributing to their flux measurement. The histograms of Fig. 8b show the same as Fig. 8a, but for the six GOODS v2.0 mosaic tiles in BViz that overlap with the ERS. Fig. 8c shows the same as Fig. 8a, but for the ERS mosaics in the IR. About 40 arcmin^2 has ∼80% of the exposure time in the ERS IR mosaics, or ∼90% of the intended IR sensitivity. The overall WFC3 UVIS – IR sensitivity is 9–18% better than predicted from the ground-based thermal vacuum tests (see §2.1 and Fig. 2), and so in essence 100% of the intended exposure time was achieved over the 50 arcmin^2 UVIS images and the 40 arcmin^2 IR images.

5. CATALOG GENERATION FROM THE 10-BAND ERS MOSAICS

5.1. *Object Finding and Detection*

All initial catalogs were generated using SExtractor version 2.5.0 (Bertin & Arnouts 1996) in single image mode. It was necessary to change the parameters in SExtractor to handle the UVIS images slightly differently than the ACS/WFC and WFC3/IR ones. This is due to several factors, both cosmetic and physical. The major difference is that galaxies appear much smoother in the IR and clumpy in the UV (see Windhorst et al. 2002 for a discussion of this effect for all Hubble types), so that star-forming regions in well-resolved galaxies can be deblended into separate objects, if the deblending is overly aggressive. Fortunately, most of these intermediate redshift galaxies are not bright in the observed UV, causing the UVIS fields to appear rather sparse, and making deblending a minor issue.

The UVIS images have a less uniform background (∼10–15% of sky), which as discussed in §4.1.1 can possibly be improved when on-orbit sky-flat calibration files become available. For these reasons, we adopted a seemingly low threshold for object detection with SExtractor, requiring 4 connected pixels that are 0.75σ above the background in the UV.

Due to the clumpy nature of the ERS objects in the UV, we convolved the UVIS image with a Gaussian kernel of FWHM of 6.0 pixels for the object detection phase only. The deblending parameter, DEBLEND_MINCONT, was set to 0.1, to assure that real objects were not over-deblended. It should be emphasized that object crowding in not an issue in these medium depth UV images, so that the use of a larger SExtractor convolution filter, a lower SB-detection threshold, and less object deblending is fully justified.

The SExtractor input parameters for the ACS images and WFC3/IR images were the same. The detection threshold was set to 1.5σ, again requiring 4 connected pixels above the threshold for catalog inclusion. The convolution filter was a Gaussian with FWHM of 3.0 pixels, and DEBLEND_MINCONT was set to 0.06. For all ten bands, the appropriate RMS maps (see §4.2.2) were used in order to correctly account for image borders (Fig. 3), as well as to properly characterize the photometric uncertainties and the effective areas for each mosaic (Fig. 8).

5.2. *Object Extraction*

Two post-processing steps were taken to clean the catalogs of residual artifacts. First, due to the relatively small number of exposures per filter, there were residual cosmic rays at the borders of the dither patterns, and in the chip gaps. These were cleaned by masking out all objects in regions where the number of exposures was less than three. Therefore the total area coverage in each filter (Table 2 & Fig. 8) is slightly different. Secondly, SExtractor will detect the diffraction spikes of bright point sources. These are removed by searching for bright objects with FWHM near the size of the PSF, and searching for surrounding objects in the catalog that are *both* highly elongated *and* oriented radially outward in sets of 4 from that compact source. Since the number of stars is not large, this is only a minor correction to the catalog, and only a few dozen diffraction spikes were found by SExtractor and removed in this way.

Magnitudes were all measured on the AB-scale using the most current zero-points available on the WFC3 website which are listed in Table 2. Both Petrosian (1976) magnitudes were measured using a Petrosian factor of 2.0, and Kron (1980) magnitudes were measured using a Kron-factor of 2.5 (SExtractor parameter MAG_AUTO). For the galaxy counts in §6.2, Kron magnitudes were used, because the correction to total magnitude — preferably using a Sersic extrapolation — is less than that typically required for a Petrosian magnitude. Within the errors, the Kron and Sersic based number counts are indistinguishable (Hill et al. 2010b). The total magnitude errors in the ERS as a function of total AB-magnitude were determined from the SExtractor errors in each filter, which are a combination of multidrizzle weight-map errors and the image shot-noise.

5.3. *ERS Sample Completeness*

Fig. 9b shows the completeness functions of the 10-band ERS images. These were derived by Monte Carlo insertion of faint point sources into the ERS images, and plotting the object recovery ratio as a function of total magnitude. In summary, the WFC3 UVIS images are ∼50% complete for point-like objects with $\gtrsim 5$-σ detections in total flux for AB$\lesssim$26.3 mag in F225W, AB$\lesssim$26.4 mag in F275W, and AB$\lesssim$26.1 mag in F336W. The WFC3 IR images are complete to AB$\lesssim$27.2 mag in F098M, AB$\lesssim$27.5 mag in F125W, and AB$\lesssim$27.2 in F160W, as listed in Table 1. The actual star counts in §6 appear indeed complete to roughly these limits in the UV, but to slightly brighter limits in the IR due to the significant object confusion of red stars with faint red background galaxies.

The actual UV galaxy counts in §6.2 turn over at a level rather close to the above UVIS point-source sensitivity limits. This is due to the in general more compact nature of the ERS objects and the extremely faint zodi sky-background in the UV. In the IR, the galaxy counts turn over at levels a little brighter than the 5-σ point-source sensitivity limits listed in Table 2. Despite the generally rather compact nature of the faint red field galaxies selected in Y_sJH, this is due to the higher zodiacal sky background values in the near-IR (see Table 2).

5.4. *Star Galaxy separation in the ERS Mosaics*

Stars and galaxies were separated as following. In each filter, the stellar locus was defined as shown in the usual plot of object FWHM versus total AB-magnitude. Fig. 10 illustrates our star-galaxy separation procedure used for the 10-band ERS images. Objects with r_e<FWHM (from Table 2) are image defects, bad pixels, and some remaining CRs. Hence, objects to the left of the black vertical lines plotted at $r_e \simeq 0\farcs07$–$0\farcs15$ FWHM are smaller than the PSF, and are discarded. Objects in the thin vertical filaments immediately larger than this are stars (plotted as thin reds dots), and they in general have FWHM$\lesssim r_e \lesssim (1+\epsilon)\times$FWHM, where $0 \lesssim \epsilon << 1$. Fig. 10 shows that stars straddle the instrumental PSF FWHM to AB$\lesssim$27 mag. Objects to the right of the black dashed slanted lines are galaxies, and they have $r_e \gtrsim (1+\epsilon)\times$FWHM, where "$1+\epsilon$" is a weak function of total S/N-ratio, as shown by the solid, nearly vertical slanted lines in Fig. 10.

Next, all ten independent ERS object catalogs — each with their independent star-galaxy separation and photometry — were merged by astrometric cross-matching. In order to maximize the 10-band information, we considered an object to be a star if it was classified as stellar in *at least three filters*. This provides robust stellar classifications, perhaps to fainter limits than can be done in single filter alone.

From the resulting ERS objects counts in Fig.

11a, we can see that the stars separate out well from the galaxies to about AB$\lesssim$25.5–26.0 mag, and somewhat fainter in the ACS BViz filters and the WFC IR filters. To these flux levels, the star counts follow a power-law rather well, as shown in Fig. 11a. The choice of three filters to require an object to be classified as a star — as opposed to all ten filters — was made because stellar SEDs do not span a large range in wavelength, and because we are merging the data from three different detectors (WFC3 UVIS CCD, ACS/WFC CCD, and the WFC3 IR detector).

6. SCIENCE RESULTS FROM THE ERS MOSAICS

6.1. *The Panchromatic ERS Star Counts to AB$\lesssim$ 26 mag*

Fig. 11a shows the star counts and galaxy number counts in the 10-band ERS images. The star-galaxy separation breaks down for AB$\gtrsim$26 mag in BVizYJH. However, for AB$\gtrsim$22 mag galaxies outnumber stars by a large margin, so the more uncertain star-galaxy separation for AB$\gtrsim$26 mag will not affect the quality of the galaxy counts. The star counts, of course, become correspondingly harder to do for AB$\gtrsim$25 mag, and so additional criteria will need to be invoked to identify faint very blue or very red stars with high confidence.

The solid black line in the F850LP panel of Fig. 10 are the spectroscopic star counts to AB$\lesssim$25 mag from the HST GRAPES and PEARS ACS grism surveys of Pirzkal et al. (2005, 2009). The GRAPES and PEARS ACS grism surveys were done over an area almost twice as large as the ERS — covering *both* GOODS-N and GOOD-S — and so it is encouraging that the Pirzkal grism star counts have the same slope as our direct-imaging ERS star counts in F850LP. (The slightly different star count amplitudes are likely due to the fact that the different Galactic latitude of the GOODS-N field was averaged into the PEARS grism star counts as well). The good agreement in star counts between the two different survey methods confirms that — as far as faint stars are concerned — our star-galaxy separation is accurate to at least AB$\simeq$25 mag.

Fig. 11b shows the ERS star count slope versus observed wavelength in the flux ranges AB$\simeq$19–25.5 mag for the 3 UV WFC3 filters, AB$\simeq$16–26 mag for the GOODS/ACS BViz filters, and AB$\simeq$15–25 mag for the 3 WFC3 IR filters, respectively. The star count slope in the three WFC3 ERS UV filters are poorly determined because of the paucity of stars seen overall in the UV. The GALEX FUV and NUV points of Xu et al. (2005) are also plotted at 153 and 231 nm, and cover AB=17–23 mag, using primary color criteria to accomplish star-galaxy separation at the 4–6" FWHM GALEX resolution.

The faint-end of the Galactic star count slope is remarkably flat at all wavelengths from the Balmer break to the near-IR, although it is rather poorly determined from the ERS data alone below the Balmer break. The values of the best fit power-law star count slope is in general of order 0.03–0.05 dex/mag, i.e. well below Euclidean value of 0.6 dex/mag. This shows that to a depth of AB$\simeq$25–26 mag at all wavelengths in the range 0.2–2 μm, the ERS images are quickly looking through most of the thick disk of our Galaxy at these latitudes ($b^{II} \simeq$–54°) in the direction of the Galactic anti-center (l^{II} =224°; Ryan et al. 2005; Beckwith et al. 2006). This trend was also seen in the red ACS imaging parallels of Ryan et al. (2005), and the red ACS GRAPES and PEARS grism observations of Pirzkal et al. (2005, 2009), respectively, each of which constrained the scale-height of Galactic L & T dwarfs to about 300–400 pc.

In the bluest three WFC3 filters F225W, F275W, and F336W, the WFC3 ERS finds only 22, 18, and 27 faint stellar candidates, respectively. Most of these stars have 10-band colors red enough to indicative of Galactic halo K–M type stars and possibly a few L & T dwarfs, but a few of the faint ERS stars are blue. The latter could be faint Galactic white dwarfs. The effective ERS UV stellar detection limit of AB$\lesssim$25 mag could trace a T=2$\times$10^{4}K white dwarf with an absolute magnitude in the range $M_{bol}\simeq$+15 to +10 mag (Harris et al. 2006) out to a distance of 1–10 kpc, respectively, assuming modest bolometric corrections. The stellar ERS objects are obviously of interest by themselves, and will be studied in more detail in a future ERS paper. It suffices to say here that the ERS data also has the potential to find faint white dwarf stars using the WFC3 UV filters, and faint K& stars and L& T dwarf through its ACS optical and WFC3 IR filters.

6.2. *The Panchromatic ERS Galaxy Counts to AB$\lesssim$ 26–27 mag*

Fig. 11c shows the ERS Galaxy count slope versus observed wavelength in the flux ranges AB$\simeq$19–25 mag for the 3 UV WFC3 filters, AB$\simeq$18–26 mag for the GOODS/ACS BViz filters, and AB$\simeq$17–25 mag for the 3 WFC3 IR filters, respectively. The GALEX FUV and NUV points of Xu et al. (2005) are also plotted at 153 and 231 nm, and cover AB=17–23 mag, again using primary color criteria to accomplish star-galaxy separation at the 4–6" FWHM GALEX resolution.

The galaxy counts show the well known trend of a steepening of the best-fit power-law slope at the bluer wavelengths, which is caused by a combination of the more significant K-correction and the shape of the galaxy redshift distribution at the selection wavelength. The galaxy count slope changes significantly from $a\simeq$0.44 dex/mag at 0.23 μm wavelength to $a\simeq$0.26 dex/mag at 1.55 μm wavelength. Hence, the galaxy counts have a slope flatter than the Euclidean value of $a\simeq$0.6 dex/mag, but below the Balmer break the UV galaxy counts are steeper than the $a \leq$0.4 dex/mag value required for their sky-brightness integral to converge, *if* they were to continue with this power-law slope for AB$\gtrsim$27 mag.

That is, the UV galaxy counts will have to turn over with a slope flatter than $\leq$0.4 dex/mag for AB$\gtrsim$27 mag. In §6.3 we confirm that they indeed do so.

6.3. *The Panchromatic Galaxy Counts for 10$\lesssim$ AB$\lesssim$ 30 mag*

Fig. 12a–12j show the galaxy number counts in the 10-band ERS images compared to a number of other panchromatic surveys at the bright end and at the faint end. At the bright end, we added the GAMA survey (Driver et al. 2009) counts in NUV+uvgriYJH, which cover AB=10–21 mag (Xu et al. 2005; Hill et al. 2010a). GAMA also uses matched aperture Kron magnitudes, but GAMAs star-galaxy separation is quite different than for the ERS, since there is a significant potential for stellar contamination due to stars dominating the number counts at brighter magnitudes. The GAMA separation makes use of r_{PSF}–r_{Petro} to determine how extended a source is, and the strong stellar locus on the (g–i) vs. (J–K) color-color diagram. A detailed discussion on the star galaxy separation methods used in the GAMA survey is given by Baldry et al. (2010).

At the faint end, we added the HUDF counts in BViz from Beckwith et al. (2006), which cover AB=24–30 mag, and the HUDF counts from the Bouwens et al. (2009) YJH data as compiled by Yan et al. (2009), which cover AB=24–30 mag. In the UV, we added WHT U-band counts and the HDF-North and South F300W counts as compiled by Metcalfe et al. (2001), the deep LBT U-band counts of Grazian et al. (2009), as well as the deep HST STIS counts of Gardner et al. (2000).

We note that the filter systems in the comparisons in each of Fig. 12a-12j are not identical, although they were chosen if every case to be as close as possible in wavelength (typically to within 0.1 dex). Hence where necessary, small but appropriate AB-mag offsets or color transformations were made between the filters and models used in each plot, following Metcalfe et al. (2001) or Windhorst et al. (1991). These corrections generally contain some color dependence. When applying them as a single AB-flux scale correction for a given survey can introduce uncertainties of order 0.1-0.2 mag in the flux-scale used, which over the entire AB=10–30 mag range shown in Fig. 12a–12j is not noticeable. However, for a detailed set of modeling in subsequent work, more subtle flux and color dependent corrections may need to be applied.

The error bars in each of the counts are Poisson, and therefore do not include effects from cosmic variance. To increase the statistics where necessary at the bright-end of each survey, bins were combined logarithmically using the local slope of the counts, following Windhorst et al. (1984). At the faint-end, the counts are not plotted in Fig. 12a–12j beyond the level where these are deemed complete. Based on Fig. 9 and 11, this occurs in general where the counts turn over significantly within the error bars. Hence, in principle, the counts should comparable over the entire flux range AB$\simeq$10–30 mag, except for the effects of cosmic variance. The latter is small for the panchromatic $\sim$116 deg^2 GAMA survey, but it could be important for the other panchromatic survey areas plotted, such as the ERS and the HUDF which are both (disjoint) parts of GOODS-S, as well as the HDF-N (in GOODS-N) plus the HDF-S and various other ground-based surveys in the U-band.

Where the panchromatic GAMA and HUDF counts in Fig. 12a–12j overlap with the panchromatic ERS counts, the agreement is in general quite good, except at the bright-end of the ERS, which suffers from cosmic variance, and from the fact that the GOODS/ERS field was chosen to be devoid of objects much brighter than AB=18 mag. As a consequence, the bright end of the ERS galaxy counts suffers somewhat from incompleteness. The same is true for the bright end of the HUDF, which suffers similarly from cosmic variance and the avoidance of objects much brighter than AB$\sim$21–22 mag when that field was selected for the ultradeep HST survey. The HUDF is adjacent to, but does not overlap with the ERS area (see Fig. 3). The BVizYJH HUDF galaxy counts are in good agreement with the ERS galaxy counts to the flux levels where the panchromatic ERS counts are considered complete (AB$\lesssim$26–27 mag in Fig. 11a).

The good agreement between these various surveys also implies that the flux scales of the panchromatic ERS counts are approximately correct. Had one of the ERS filter zeropoints been off significantly ($\gtrsim$0.1–0.2 mag), we would have noticed this as a significant offset between the counts. Note this argument only holds for the counts at AB$\gtrsim$20 mag, as these cover the same general area of sky in the GOODS-S field, so that cosmic variance effects likely affect these counts similarly over such scales ($\lesssim$30%, Somerville et al. 2004).

6.4. *Modeling the Panchromatic Galaxy Counts for 10$\lesssim$ AB$\lesssim$ 30 mag*

Fig. 12a–12j over-plots simple galaxy evolution models described by Driver et al. (1998). In summary, these contain the best available local panchromatic LFs in ugrizYJHK from the MGC survey by Hill et al. (2010b), and in the UV using the GALEX LFs of Robotham & Driver (2010). These LFs will be updated in future work with GAMA redshifts from the 3 year AAT survey that was concluded in May 2010. This GAMA data set is 99% redshift-complete for $r_{Petro}\lesssim$19.4 mag, and will provide high-fidelity, matched-volume panchromatic LFs, which will be essential to interpret the higher redshift ERS work. Robotham et al. (2010) give further details on the GAMA redshift survey.

Based on these currently available, best panchromatic local LF's, Fig. 12a–12j show from AB=10–30 mag either a pure luminosity evolution model (PLE) with e(z) = 2.5 log10[(1+z)$^{\beta}$] with PLE exponent β=1 (dotted lines), *or* a number density evo-

lution (NDE) model with n(z) = n_o $[(1+z)^\gamma]$ with exponent γ=1 (short-dashed lines, *or* a combination of both models indicated by *both* β=γ=1 (long-dashed lines). The solid lines show in all cases the non-evolving model (β=γ=0). These models are described in more detail by Driver et al. (1995) and Cohen et al. (2003).

Over the entire flux range AB=10-30 mag, Fig. 12a–12j show that no single PLE model fits all the available galaxy count data, since there is not enough volume at high redshift to make any PLE model fit the high observed counts, especially in the visual to near-IR (fig. 12d–12j). This means that one has to invoke number density evolution as well, *i.e.*, $\beta \gtrsim 1$ and some modest amount of luminosity evolution for $\gamma \gtrsim 0$. *However, none of the simple PLE+NDE models fits the panchromatic galaxy counts either in all 10 bands simultaneously over the entire observed range AB=10–30 mag,* not even with the best available panchromatic local LF from GAMA (Hill et al. 2010).

In particular, Fig. 12d–12j show that at the faint-end of the galaxy counts in YJH there exists a significant excess in object numbers. These could be either an additional population at high redshifts, and/or — more likely — lower luminosity objects at lower redshifts. A detailed discussion of these possibilities is beyond the scope of the current paper, but the reader is referred to Bouwens et al. (2009) and Yan et al. (2009) for a discussion of some of these possibilities. More realistic models would be ones in which the faint-end Schechter LF slope α *also* evolves with redshift, as has been suggested by *e.g.*, Ryan et al. (2007) and Khochfar et al. (2007). In particular, the faint-end slope α has too steepen significantly at higher redshifts, which was suggested by *e.g.*, Yan & Windhorst (2004), Ryan et al. (2007) and Hathi et al. (2010). This will be subject of a future, more detailed model fitting paper of the panchromatic galaxy counts. *For now, we conclude that any more sophisticated model of galaxy assembly — including hierarchical merging and or downsizing with or without feedback — will need to at least reproduce the overall constraints provided by the current panchromatic galaxy counts from 10$\lesssim$ AB$\lesssim$ 30 mag over a full factor of 10 in wavelength.*

6.5. *Interesting Classes of Objects in the Panchromatic ERS mosaics*

Fig. 13 shows several panchromatic postage stamps of lower redshift early-type galaxies in the ERS with nuclear star-forming rings, bars, or other interesting nuclear structure. Each postage stamp is displayed at a slightly different color stretch, that best brings out the UV nuclear structure. (Rutkowski et al. (2010) present examples of ellipticals at z$\simeq$0.3–1 with various amounts of UV-excess flux. These galaxies are red and relatively featureless in the optical, but show considerable emission in the UV, which is not all point-like. Hathi et al. (2010) and Ryan et al. (2010) present ERS samples of faint UV-dropouts and very high redshift red galaxies, respectively. Many more such studies can be done with the ERS data.

Fig. 14 shows panchromatic postage stamps of objects with interesting morphological structure in the 10-band ERS color images of the CDF-S, yielding high signal-to-noise ratio detections of galaxies resembling the main cosmological parameters H_0 , Ω, ρ_o, w, and Λ, respectively. The panchromatic galaxy morphology and structure in the ERS images is so rich, that a patient investigator can find galaxies of nearly any appearance in the epoch z$\simeq$1–3. This is because galaxy merging was in full swing in this epoch.

7. SUMMARY AND CONCLUSIONS

In this paper, we presented the new HST WFC3 Early Release Science (ERS) observations in the GOODS-South field. We presented the scientific rationale of this ERS survey, the data taking plus data reduction procedures of the panchromatic 10-band ERS mosaics. We described in detail the procedure of generating object catalogs across the 10 different ERS filters.

The new WFC3 ERS data provide calibrated, drizzled mosaics in the mid-UV filters F225W, F275W, and F336W, as well as in the near-IR filters F098W (Y_s), F125W (J), and F160W (H) in 1–2 HST orbits per filter. Together with the existing HST Advanced Camera for Surveys (ACS) GOODS-South mosaics in the BVi'z' filters, these panchromatic 10-band ERS data cover 40–50 square arcmin at 0.″07–0.″15 FWHM resolution and 0.″090 multidrizzled pixels to depths of AB$\lesssim$ 26.0–27.0 mag (10-sigma) for point sources and AB$\lesssim$ 25.5–26.5 mag for compact galaxies.

We also described the high quality star-galaxy separation made possible by the superb resolution of HST/WFC3 and ACS over a factor of 10 in wavelength to AB$\lesssim$ 25–26 mag from the UV to the near-IR, respectively, as well as the reliability and completeness of the object catalogs from the ERS mosaics. Our main scientific results are:

1) We present the resulting Galactic star counts and galaxy counts in 10 different filters. From the ERS data, these could be accurately determined from AB$\simeq$19 mag to AB$\lesssim$ 26 mag over a full factor of 10 in wavelength from the mid-UV to the near-IR.

2) Both the Galactic stars counts and the galaxy counts show mild but significant trends of decreasing count slopes from the mid–UV to the near-IR over a factor of 10 in wavelength.

The faint-end of the Galactic star count slope is remarkably flat at all wavelengths from the Balmer break to the near-IR. The values of the best fit power-law star count slope is in general of order 0.03–0.05 dex/mag above the Balmer break, i.e. well below Euclidean value of 0.6 dex/mag. This shows that to a depth of AB$\simeq$25–26 mag at all wavelengths in the range 0.2–2 μm, the ERS images are

quickly looking through most of the thick stellar disk of our Galaxy at intermediate latitudes.

The galaxy count slope changes significantly from $a \simeq 0.44$ dex/mag at 0.23 μm wavelength to $a \simeq 0.26$ dex/mag at 1.55 μm wavelength, showing the well known trend of a steepening of the best-fit power-law slope at the bluer wavelengths. This is caused by a combination of the more significant K-correction and the shape of the galaxy redshift distribution at the selection wavelength.

3) We combine the 10-band ERS counts with the panchromatic GAMA counts at the bright end ($10 \lesssim$ AB $\lesssim 20$ mag), and with the ultradeep BVizYJH HUDF counts and other available HST UV counts at the faint end ($24 \lesssim$ AB $\lesssim 30$ mag). *The galaxy counts are now well measured over the entire flux range $10 \lesssim AB \lesssim 30$ mag over nearly a of 10 in wavelength.*

4) We fit simple galaxy evolution models to these panchromatic galaxy counts over this entire flux range $10 \lesssim$ AB $\lesssim 30$ mag, using the best available 10-band local galaxy luminosity functions (LFs) from the GAMA survey (Hill et al.2010a), as well as simple prescriptions of luminosity and/or density evolution. *While these models can explain each of the 10-band counts from $10 \lesssim AB \lesssim 30$ mag well, no single one of these simple PLE+NDE models can explain the counts over this entire flux range in all 10 filters simultaneously.* Any more sophisticated model of galaxy assembly, including hierarchical merging and or downsizing with or without feedback, will need to at least reproduce the overall constraints provided by the current panchromatic galaxy counts from $10 \lesssim$ AB $\lesssim 30$ mag over a full factor of 10 in wavelength.

These surveys also emphasize the need for extending this work to AB $\gtrsim 30$ mag and beyond at longer wavelengths, which the James Webb Space Telescope will do for wavelengths in the range 1–28 μm after its launch in 2014. The unique abilities of WFC3 to do deep UV imaging will need to be explored fully before that time.

5) We show examples of interesting panchromatic faint galaxy structure in intermediate redshift objects, including early-type galaxies with nuclear star-forming rings and bars, and/or weak AGN activity, and some objects of other unusual appearance.

The panchromatic ERS data base is very rich in structural information at all rest-frame wavelengths where young or older stars shine during the peak epoch in the cosmic star-formation rate ($z \simeq 1$–2), and constitutes a unique new HST data base for the community to explore in the future.

This paper is based on Early Release Science observations made by the WFC3 Scientific Oversight Committee. We are grateful to the Director of the Space Telescope Science Institute, Dr. Matt Mountain, for generously awarding Director's Discretionary time for this program. We thank Drs. Neill Reid, Ken Sembach, Ms. Tricia Royle, and the STScI OPUS staff for making it possible to have the ERS data optimally scheduled. We also thank WFC3 IPT and the GSFC WFC3 Project for their very hard dedicated work since 1998 to make this wonderful instrument work, and for their timely delivery of the essential hardware and software to make the acquisition and reduction of the new WFC3 data possible. We also thank the entire GOODS team, and in particular Drs. Norman Grogin and Mauro Giavalisco for making the exquisite GOODS v2.0 mosaics available.

Support for HST program 11359 was provided by NASA through grants GO-11359.0*.A from the Space Telescope Science Institute, which is operated by the Association of Universities for Research in Astronomy, Inc., under NASA contract NAS 5-26555. RAW also acknowledges support from NASA JWST Interdisciplinary Scientist grant NAG5-12460 from GSFC. HY is supported by the long-term fellowship program of the Center for Cosmology and AstroParticle Physics (CCAPP) at The Ohio State University.

We thank the STS-125 astronauts for risking their lives during the Shuttle Servicing Missions SM4 to Hubble, and for successfully installing WFC3 into HST in May 2009. We dedicate this paper to the memory of the STS-107 Columbia Shuttle astronauts and of Dr. Rodger Doxsey, who during their lives contributed so much to the Space Shuttle and the Hubble Space Telescope projects.

REFERENCES

Abraham, R. G.; Ellis, R. S., Fabian, A. C., Tanvir, N. R., & Glazebrook, K. 1999, MNRAS, 303, 641
Abraham, R. et al. 2007, ApJ, 669, 184
Afonso, J., Mobasher, B., Koekemoer, A., Norris, R. P., & Cram, L. 2006, AJ, 131, 1216
Baldry, I. K. et al. 2010, MNRAS, 404, 86
Beckwith, S. V., Stiavelli, M., Koekemoer, A. M., et al. 2006, AJ, 132, 1729
Bertin, E. & Arnouts, S. 1996, A&AS, 117, 393
Bond, H. E., & Kim Quijano, J., et al. 2007, "Wide Field Camera 3 Instrument Handbook, Version 1.0" (Baltimore: STScI)
Bruzual, G., & Charlot, S. 2003, MNRAS, 344, 1000
Chandar, R., et al. 2010, ApJ, submitted
Cohen, S. H., Windhorst, R. A., Odewahn, S. C., Chiarenza, C. A. T., & Driver, S. P. 2003, AJ, 125, 1762
Cohen, S. H., et al. 2006, ApJ, 639, 731
Cohen, S. H., et al. 2010, in preparation
Conselice, C. J. Bershady, M. A., Dickinson, M., & Papovich, C. 2003, AJ, 126, 1183
Crockett, R. M., et al. 2010, ApJ, submitted
De Lucia, G., Springel, V., White, S. D. M., Croton, D., & Kauffmann, G. 2006, MNRAS, 366, 499
Di Matteo, T., Springel, V., & Hernquist, L. 2005, Nature, 433, 604
Dickinson, M., Papovich, C., Ferguson, H. C., & Budavri, T. 2003, ApJ, 587, 25
Dickinson, M., et al. 2004, ApJ, 600, L99
Driver, S. P., Windhorst, R. A., Ostrander, E. J., Keel, W. C., Griffiths, R. E., & Ratnatunga, K. U. 1995, ApJL, 449, L23

Driver, S. P., Fernandez-Soto, A., Couch, W. J., Odewahn, S. C., Windhorst, R. A., Phillipps, S., Lanzetta, K., & Yahil, A. 1998, ApJL, 496, L93
Driver, S. P., et al. 2009, Astron. & Geophys. 50, 5.12
Dopita, M. A., et al. 2010, ApJ, 710, 964
Ferreras, I., et al. 2009, ApJ, 706, 158
Gardner, J. P., Satyapal, S. 2000, AJ, 119, 2589
Gardner, J. P., Brown, T. M., Ferguson, H. C. 2000, ApJL, 542, L79
Giacconi, R., et al. 2002, ApJS, 139, 369
Giavalisco, M., Ferguson, H. C., Koekemoer, A. M., Dickinson, M. et al. 2004, ApJ, 600, L93
Grazian, A., Menci, N., Giallongo, E. et al. 2009, A& A, 505, 1041
Grogin, N., et al. 2009, GOODS v2.0 mosaics, priv. comm.
Harris, H. C., Munn, J. A., Kilic, M., et al. 2006, AJ, 131, 571
Hathi, N. P., et al. 2008, AJ, 135, 156
Hathi, N. P., et al. 2010, ApJ, submitted (arXiv:1004.5141)
Hill, D. T., Driver S. P., Cameron E., Cross N. J. G., Liske J., & Robotham, A. 2010a, MNRAS, 404, 1215
Hill, D. T., et al. 2010b, MNRAS, submitted (http://star-www.st-and.ac.uk/~dth4/GAMA2v5.pdf)
Hopkins, P. et al. 2010, ApJ, 715, 202
Hopkins, P., Hernquist, L., Cox, T., di Matteo, T., Robertson, B., & Springel, V. ApJS, 163, 1
Kellermann, K. I., Fomalont, E. B., Mainieri, V., Padovani, P., Rosati, P., Shaver, P., Tozzi, P., & Miller, N. 2008, ApJS, 179, 71
Koekemoer, A. M., Fruchter, A. S., Hook, R. N., & Hack, W. 2002, in "The HST Calibration Workshop: Hubble after the Installation of the ACS and the NICMOS Cooling System", p. 337, Eds. S. Arribas, A. Koekemoer, & B. Whitmore. (Baltimore: STScI)
Komatsu, E., et al. 2010, arXiv, 1001.4538
Kron, R. G. 1980, ApJS, 43, 305
Labbé, I., et al. 2003, AJ, 125, 1107
Law, D. R., et al. 2007, ApJ, 656, 1
Law, D. R., et al. 2009, ApJ, 697, 2057
Lilly, S., J., et al. 1998, 1998, ApJ, 500, 75
Maybhate, A., et al. 2010, "ACS Instrument Handbook", Version 9.0 (Baltimore: STScI)
Malhotra, S., et al. 2005, ApJ, 626, 666
Melbourne, J., et al. 2005, ApJ 625, L27
Nonino, M., Dickinson, M., Rosati, P. et al. 2009, ApJS, 183, 244 (0906.4250v1)
Petrosian, V. 1976, ApJ, 209, L1
Pirzkal, N., et al. 2004, ApJS, 154, 501
Pirzkal, N., et al. 2005, ApJ, 622, 319
Pirzkal, N., et al. 2009, ApJ, 695, 1591
Rhoads, J. E., et al. 2009, ApJ, 697, 942
Robotham, A., et al. 2010, PASA, 27, 76
Robotham, A., & Driver, S. P. 2010, MNRAS, submitted
Ryan, R. E., Jr., Hathi, N. P., Cohen, S. H., & Windhorst, R. A. 2005, ApJL, 631, L159
Ryan, R. E., Jr., et al. 2007, ApJ, 668, 839
Ryan, R. E. Jr., Cohen, S. H., Windhorst, R. A., & Silk, J. 2008, ApJ, 678, 751
Ryan, R. E., Jr., et al. 2010, ApJ, submitted
Scannapieco, E., Silk, J., & Bouwens, R. 2005, ApJL, 635, L13
Silk, J., & Rees, M. J., 1998, A&A, 331, L1
Somerville, R. S., 2004, ApJL, 600, L171
Steinbring, E., et al. 2004, ApJS 155, 15
Straughn, A. N., et al. 2008, AJ, 135, 1624
Straughn, A. N., et al. 2009, AJ, 138, 1022
Straughn, A. N., et al. 2010, ApJ, submitted
Vanzella, E. et al. 2005, A&A, 434, 53
Windhorst, R. A., van Heerde, G. M., & Katgert, P. 1984, A&AS, 58, 1
Windhorst, R. A., et al. 1991, ApJ, 380, 362
Windhorst, R. A., et al. 2002, ApJS, 143, 113
Windhorst, R. A., Hathi, N. P., Cohen, S. H., Jansen, R. A. Kawata, D., Driver, S. P., & Gibson, B. 2008, J. Adv. Space Res., 41, 1965 (astro-ph/0703171)
Wong, M. H., Pavlovsky, C., & Long, K. et al. 2010, Wide Field Camera 3 Instrument Handbook, Version 2.0 (Baltimore, STScI)
Xu, K. et al. 2005, ApJ, 619, L11
Yan, H., Dickinson, M., Eisenhardt, P. R. M., Ferguson, H. C.; Grogin, N. A., 2004, ApJ, 616, 63
Yan, H., Dickinson, M., Stern, D., Eisenhardt, P. R. M. et al. 2005, ApJ, 634, 109
Yan, H., Windhorst, R., Hathi, N., Cohen, S., Ryan, R., O'Connell, R., McCarthy, P. 2010, ApJ, resubmitted (astro-ph/0910.0077)
Yan, H., et al. 2010, ApJ, submitted

8. APPENDIX A. THE WAVELENGTH-DEPENDENT UVIS GEOMETRICAL DISTORTION CORRECTION

Given the issues related to the GDC discussed in §4.2.2, it was apparent that some astrometric residuals remained — at the level of $\lesssim$2–3 multidrizzled pixels — that were a function of position across both UVIS detectors, after the shifts and rotations had been removed. A *worst case* is shown in the lower left panel of Fig. 4a. These residuals were apparent between the three UVIS filters, *as well as* relative to the GOODS astrometric frame. At the time of the data reduction, the best available Instrument Distortion Coefficients (IDCtab's; file t982101i_uv_idc.fits) — which are used for the GDC — had been created using the WFC3 SMOV $F606W$ data *alone* (see URL[29]). This GDC did *not yet* include any wavelength-dependent distortion terms, though these will be measured later in Cycle 17 or beyond (see URL[30]), and distributed to the community by the WFC3 instrument team. Since our WFC3/UVIS data is all taken at wavelengths below 3500 Å, it is likely that the remaining astrometric residuals are indicative of the absence of these color-dependent terms in the currently existing GDC tables. The wavelength-dependent terms of the GDC come from the different index of refraction of the glass optics and filters in the UVIS channel of WFC3. This is in addition to the first–third order geometrical distortion coefficients, which results from the CCD tilt (which was necessary to minimize internal reflections), and from other reflective optics, and are therefore largely wavelength-independent.

The ultimate goal of the UVIS part of the WFC3/ERS is to create images in F225W, F275W, and F336W filters at the same pixel scale (0.″030 per pixel) and astrometric grid as the GOODS ACS images (Giavalisco et al. 2004) of the same portion of the Chandra Deep Field South. As discussed in §2, the eight ERS UVIS pointings were designed to overlap with each other, in order to achieve the best possible astrometric precision. After the extensive astrometric work described above, it turned out that we had reached the limit of what was possible with the present *wavelength-independent* geometrical distortion solution. We were able to align all UVIS images such that the *average* object was well aligned with the GOODS B-band image. However, objects near the individual UVIS field edges were not well aligned (lower left panel of Fig. 4a). Fig. B.1 on page 273 of the WFC3 Instrument Handbook (Wong et al. 2010) also suggests that in these locations

[29] http://www.stsci.edu/hst/wfc3/idctab_lbn

[30] http://www.stsci.edu/hst/wfc3/STAN_09_2009

the geometrical distortion is the largest. This was most noticeable on the few stars in the overlap regions between pointings, as Fig. 4a demonstrated.

Some of these stars also showed significant proper motion between the original 2004–2007 GOODS observations and the 2009 ERS observations, complicating their use as astrometric fiducials. This is quite visible as large color offsets in some of the ERS bright star images in the very high resolution versions of Fig. 5a–5b, available on the *URL* quoted in the Figure caption). In attempting to create a 0.″030 per pixel UVIS mosaic, the stars in the overlap regions of the 8 UVIS pointings were somewhat elongated (Fig. 4a), even though the exposures from the same UVIS orbit were well aligned — *i.e.*, having round stars and astrometric residuals to a fraction of a pixel — *and* even though each pointing was well matched to the GOODS frame. In other words, even after correcting the WCS in the FITS headers for *both* the relative *and* the absolute position deviations, there still remained some astrometric residuals primarily at the field edges, that we suspect are likely due to the as yet unmeasured wavelength dependence of the GDC (Fig. 4b).

Fig. 4b shows the astrometric residuals for four of our ERS pointings in the F336W filter (visits 25, 26, 29, 30). Each frame within a visit was registered using the multidrizzle scripts of Koekemoer (2002), which CR-cleaned and cross-correlated the images, to revise the FLT image WCS header keywords, as described in §4.2.1. These images were then drizzled with PIXFRAC=1.0 to a scale of 0.″030 per pixel and to a position angle of 0 degrees (final_rot=0). The PA(V3) was 111 degrees. Catalogs were then created with SExtractor (Bertin & Arnouts 1996), which were in turn matched in equatorial coordinates to a similar catalog made from the GOODS-South B-band image (GOODS v2.0; Giavalisco et al. 2004; Grogin 2009, priv. comm.). Note that *all four* visits in Fig. 4b show similar bimodal residuals, suggesting that this is a systematic error. We suspect that this is due to the wavelength-dependent geometrical distortion in the UV, since the only currently available distortion solution was measured in F606W. Since two distinct blobs of points occur in *similar locations in all four panels of Fig. 4b,* the multidrizzle images of objects seen in *only one* pointing — which includes 80–90% of the total ERS area (see Fig. 3 and 8a) — *are* round at 0.″090 pixel sampling. However, the images of the brighter objects in the overlap areas between mosaic pointings — 10–20% of the total area — are not always completely round, as shown in Fig. 4a.

When Multi-drizzling the four exposures, each individual object is well aligned with itself. However, in the WFC3 field corners, an object can be offset from the GOODS WCS by ±0.″1–0.″2 (Fig. 4a–4b). In the area of field overlap, an object in the ERS image corners or at a visit's field edges can thus be misaligned with itself by ∼0.″1–0.″2, and therefore be elongated (see Fig. 4a), but still be *on average* on top of the GOODS v2.0 WCS. In other words, with the *current* wavelength-independent GDC and multidrizzle, we cannot have it both ways for a given object in the image borders of the ERS mosaic, until the wavelength-dependent GDC has been fully measured in the UV, *and* a sufficient number of dither-points is available to take full advantage of the full 0.″0.0395 pixel sampling of the WFC3 UVIS images. This is at the moment not the case. Therefore, in this paper we use the total-flux measurements from the UVIS images that were multidrizzled at 0.″090/pixel, and use large enough apertures that the total flux measurements are reliable.

Table 1. Filters, Exposure Times, & Depths of the WFC3 ERS & GOODS-S ACS data.

Channel	GRISM	GRISM	Filter1	Filter2	Filter3	Filter4	TOTAL ORBITS
WFC3/UVIS	G280		F225W	F275W	F336W		
Orbits	--		2	2	1		5x8 = 40 Direct
Depth (AB)	--		26.3	26.4	26.1		
nJy	--		110	100	132		
ACS/WFC	G800L		F435W	F606W	F775W	F850LP	
Orbits	PEARS		3	2.5	2.5	5	8x20=160 GOODS
Depth (AB)	27.0		28.5	28.5	27.8	27.3	
nJy	58		14	14	27	44	
WFC3/IR	G102	G141	F098M	F125W	F160W		
Orbits	2	2	2	2	2		6x10= 60 Direct
Depth (AB)	25.2	25.5	27.2	27.5	27.2		1x 4= 4 Grism
nJy	230	230	48	36	48		Sub = 64
TOTAL WFC3 ERS ORBITS				(Aug.--Oct. 2009)			104
TOTAL ACS GOODS ORBITS inside ERS				(2003--2007)			160
TOTAL ERS ORBITS				(2003--2009)			264

Notes to Table 1:

The listed depth is the 50% completeness for 5-sigma detections in total SExtractor AB-magnitudes for typical compact objects at this flux level (circular aperture with 0.″4 radius; 0.50 arcsec^2 aperture), as derived from Fig. 9. For spectral continuum detection in the G102 and G141 grisms, these limits are about 2.0–1.8 mag brighter, respectively. We note that the pre-flight WFC3 ETC sensitivity values were up to 0.15–0.3 mag more conservative in both the UVIS and the IR than the in-flight values observed here in Table 1a and Fig. 9, as also shown in Fig. 2.

Table 2. ERS Filters, PSFs, Zero-points, Sky-background, and Effective Area

HST-Instrument /Mode	ERS Filter	Central Lambda (mum)	Filter FWHM (mum)	PSF FWHM (")	Zeropoint (AB-mag@ 1e-/sec)	Sky-background mag/(")^2	Effective Area (arcm^2)
WFC3/UVIS	F225W	0.2341	0.0547	0.092	24.06	25.46	53.2
WFC3/UVIS	F275W	0.2715	0.0481	0.087	24.14	25.64	55.3
WFC3/UVIS	F336W	0.3361	0.0554	0.080	24.64	24.82	51.6
ACS/WFC	F435W	0.4297	0.1038	0.080	25.673	23.66	72.4
ACS/WFC	F606W	0.5907	0.2342	0.074	26.486	22.86	79.2
ACS/WFC	F775W	0.7764	0.1528	0.077	25.654	22.64	79.3
ACS/WFC	F850LP	0.9445	0.1229	0.088	24.862	22.58	80.3
WFC3/IR	F098M	0.9829	0.1695	0.129	25.68	22.61	44.8
WFC3/IR	F125W	1.2459	0.3015	0.136	26.25	22.53	44.7
WFC3/IR	F160W	1.5405	0.2879	0.150	25.96	22.30	44.7

Note 1: The panchromatic PSF FWHM was measured from ERS stars as in Fig. 7, and includes the contribution form the OTA and its wavefront errors, the specific instrument pixel sampling or Modulation Transfer Function (MTF).
Note 2: The WFC3 zero-points are in AB magnitudes for 1.0 e^- /sec from this URL[31].
Note 3: The GOODS BViz sky-background values are from Hathi et al. (2008).
Note 4: The effective areas used in this paper are in units of arcminutes squared for the effective number of WFC3 or ACS tiles available and used.
Note 5: The GOODS v2.0 BVi'z' data release is from this URL[32].
Note 6: The panchromatic effective ERS area was derived from Fig. 8 for the WFC3 mosaics and the relevant GOODS tiles.

[31] http://www.stsci.edu/hst/wfc3/phot_zp_lbn

[32] http://archive.stsci.edu/pub/hlsp/goods/v2/h_goods_v2.0_rdm.html

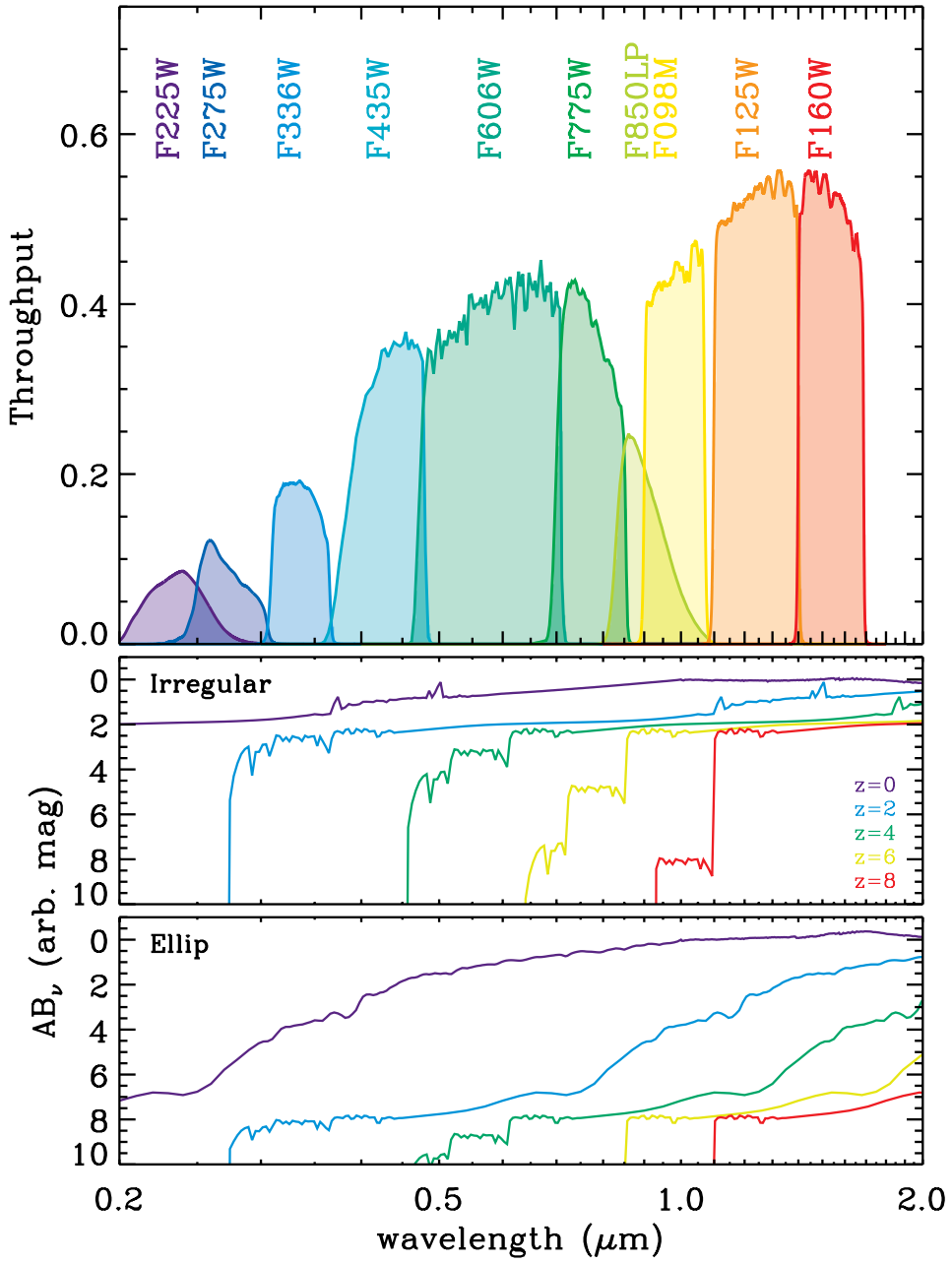

Fig. 1a. (TOP panel) The full panchromatic HST/WFC3 and ACS filter set used in the ERS imaging of the GOODS CDF-South field. Plotted is the overall system throughput, or the HST Optical Telescope Assembly throughput OTA × filter transmission T × detector QE. (MIDDLE and BOTTOM panels) Spectral energy distributions for two model galaxies with ages of 0.1 and 1 Gyr and redshifts of z=0, 2, 4, 6, 8, are shown as black, blue, green, yellow, and red curves, respectively. These show that the UVIS filters sample the Lyman-α forest and Lyman continuum breaks, while the near-IR filters will probe the 4000 Å and Balmer breaks at these redshifts. Additional photometry is available from ground-based VLT K-band imaging, and Spitzer/IRAC imaging at 3.5, 4.5, 5.6 and 8.5 micron.

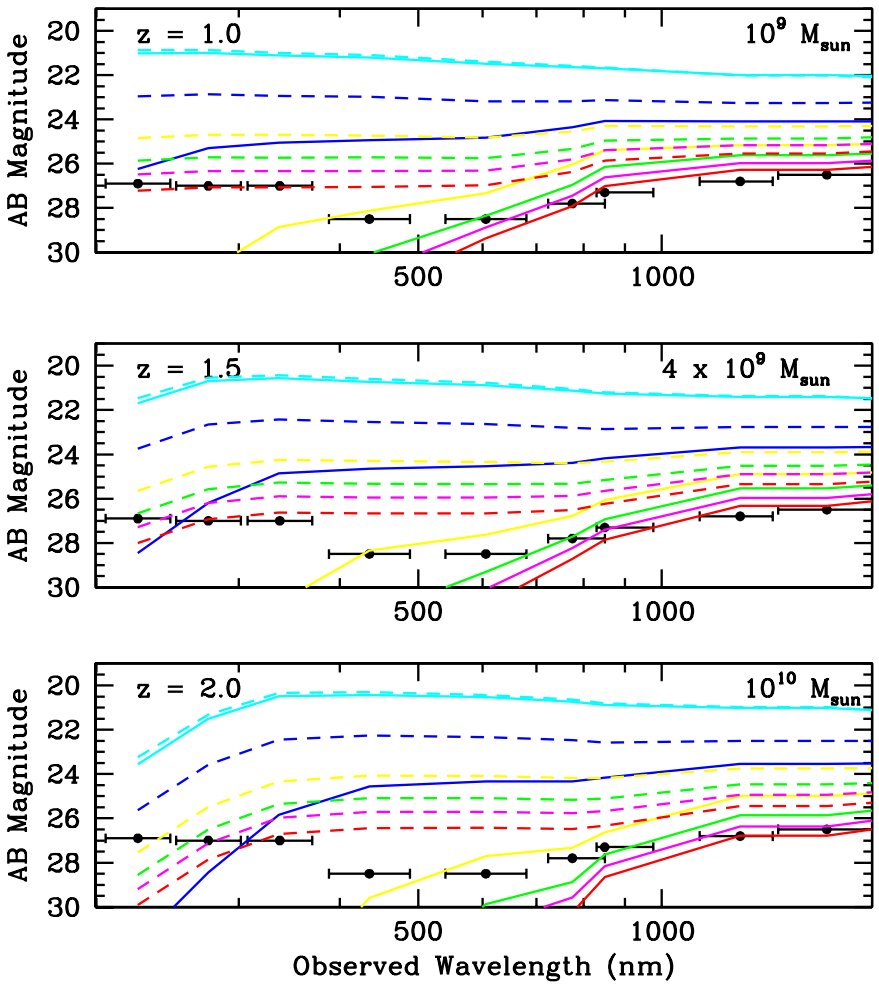

Fig. 1b. Mass sensitivity of the WFC3 ERS filters used. The three panels show the depth of the WFC3 ERS images as horizontal bars, compared to evolving galaxy models of different masses at three redshifts. The top panel is for z=1 and a stellar mass of 10^9 $M_\odot$. The solid lines represent nearly instantaneous bursts, and the dashed lines are for declining star-formation with a 1 Gyr e-folding time. The colors refer to ages of 10, 100, 500, 1000, 1400, 2000, and 3000 Myrs from cyan to red. The center panel shows similar models at z=1.5 for 4×10^9 $M_\odot$, while the lower panel is for z=2 and masses of 10^{10} $M_\odot$. At z=1, the WFC3 ERS reaches masses of 0.02 M^* for reasonable star-formation histories. Both the flux scale and the wavelength scale are logarithmic, illustrating WFC3's exquisite panchromatic coverage and sensitivity in probing the stellar masses of galaxies through its IR channel, and the star-formation in galaxies through its UVIS channel.

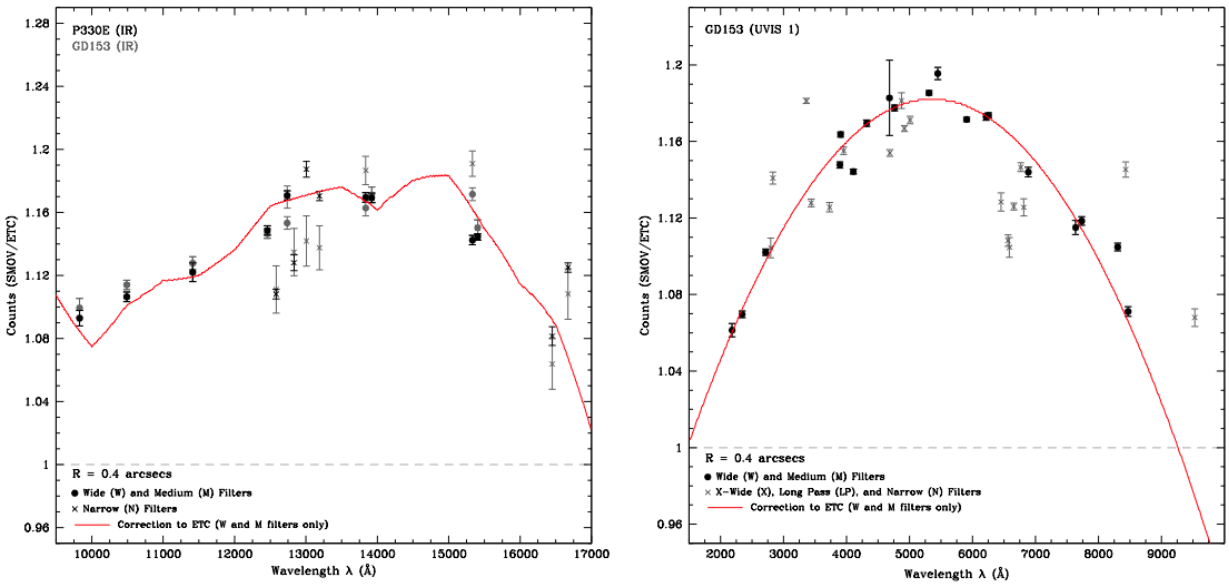

Fig. 2. On average, the on-orbit WFC3 UVIS sensitivity is 6–18% higher than the predicted pre-launch sensitivity from the ground-based thermal vacuum test (2a; left panel), and the on-orbit WFC3 UVIS sensitivity is 9–18% higher (2b; right panel).

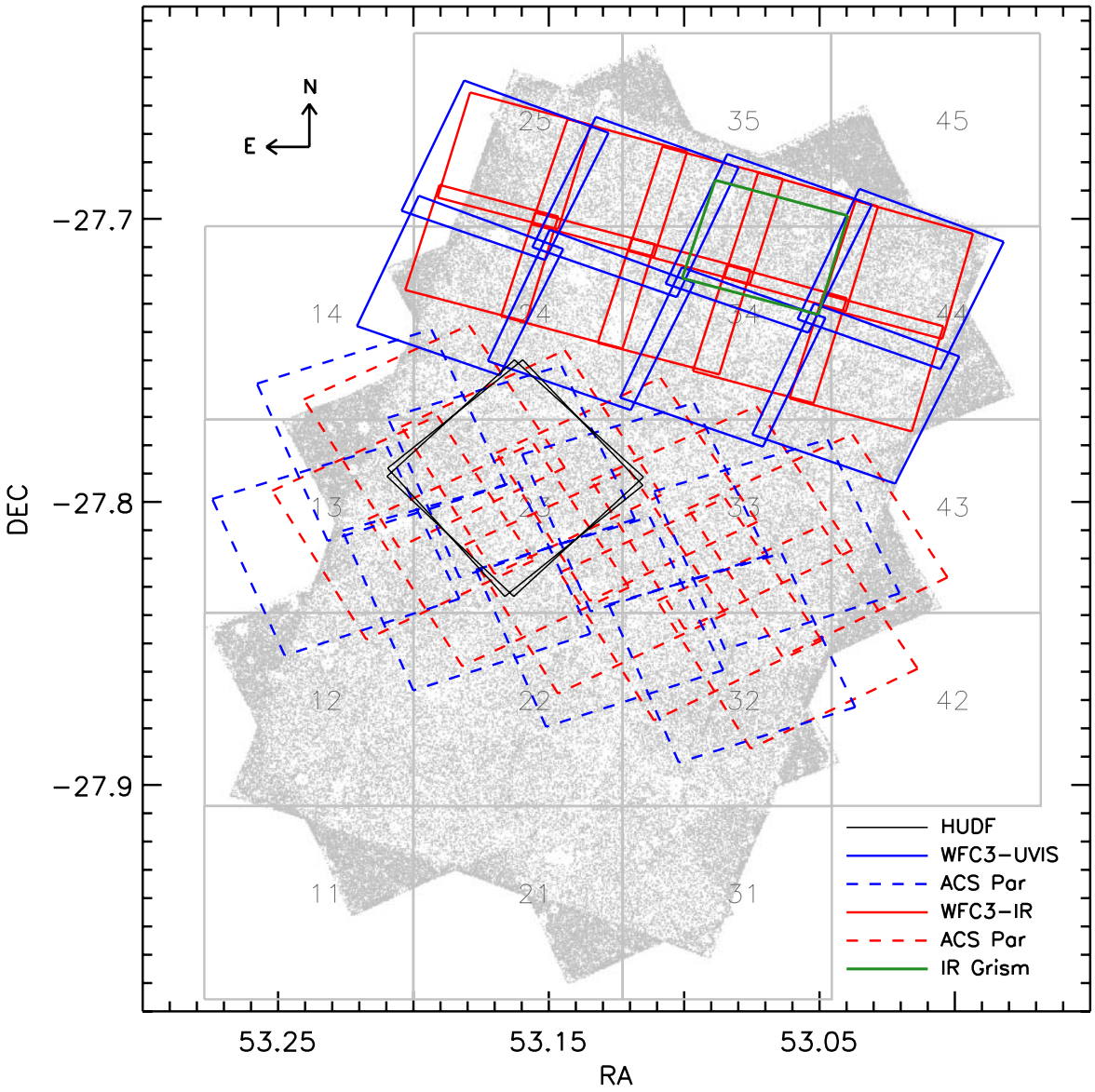

Fig. 3. Layout of the GOODS CDF-South field and its WFC3 ERS visits footprint. The 4×2 ERS UVIS mosaic is superposed in blue, and the 5 ×2 ERS IR mosaic is superposed in red. The UVIS fields are numbered from left to right, with UVIS fields 1–4 in the top row and UVIS fields 5–8 in the bottom row. The IR fields are numbered from left to right, with IR fields 1–5 in the top row and UVIS fields 6–10 in the bottom row. The dashed blue and green boxes indicate the location of the ACS parallels to the ERS WFC3 images. The ERS IR G102 and G141 grism field is shown by the green box, and overlaps with one of the PEARS ACS G800L grism field. The black box shows the ACS Hubble Ultra Deep Field in the CDF-South. The ERS program was designed to image the upper ∼20% of the GOODS-South field in six new WFC3 filters: F225W, F275W, and F336W in the UVIS channel, and F098M, F125W, and F160W in its IR channel. Further details are given in Tables 1–2. The exact pointings coordinates and observing parameters for all pointings in HST ERS program 11359 can be obtained from this URL[33].

[33] //www.stsci.edu/observing/phase2-public/11359.pro

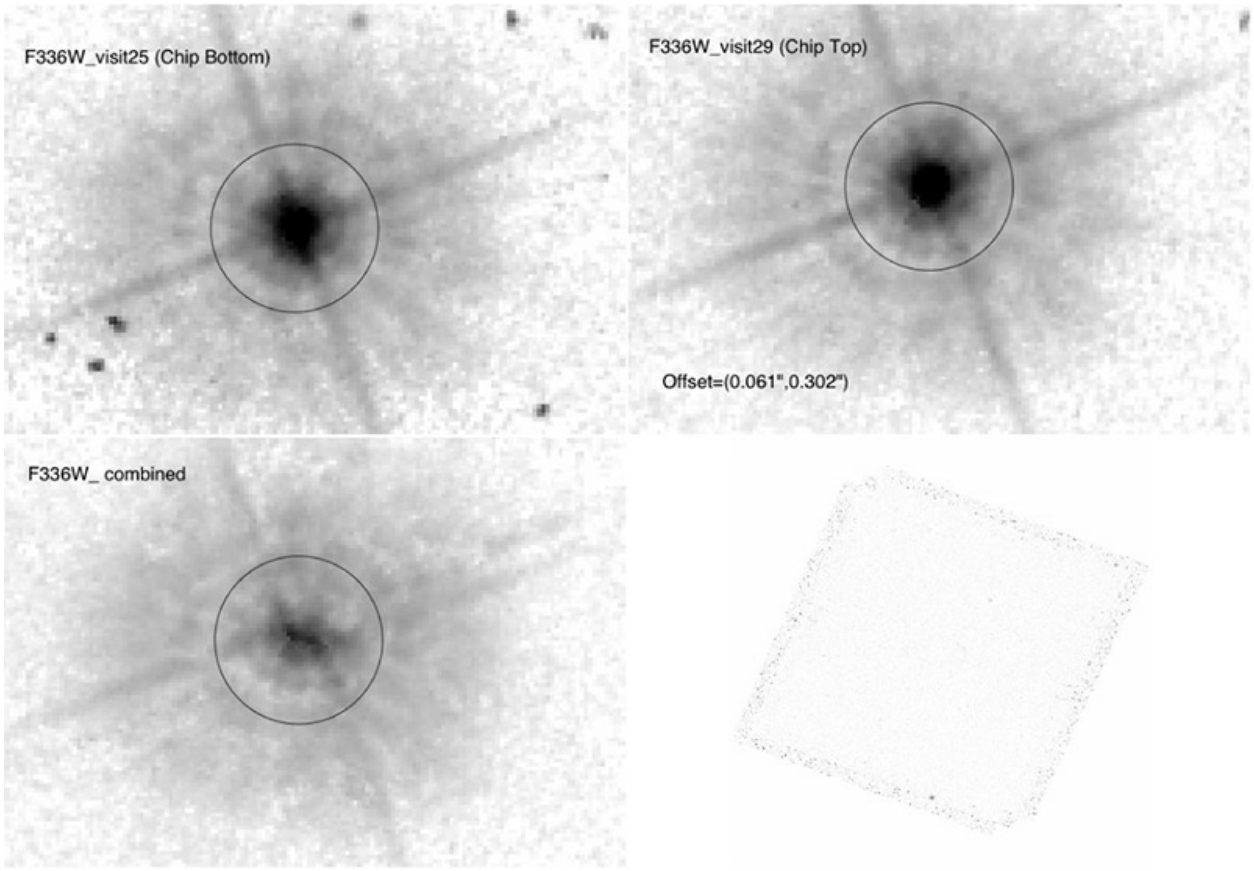

Fig. 4a. Star imaged in the overlap region (lower right panel) between UVIS visit 25 (upper left panel) and visit 26 (upper right panel) in the F336W filter. While the star is properly processed by multidrizzle in these *individual* visits (*i.e.*, its images are round in the upper left and upper right panels), it is clearly displaced by (0.″061, 0.″301) in its WCS location between these two visits. This is due to the wavelength-dependent geometrical distortion correction (GDC), which results in this star — and some other objects in the mosaic border regions — being elongated by approximately this amount when a multidrizzle is done of *all available* pointings, as can be seen in the lower left panel. A full wavelength-dependent GDC will make the images in the border regions round as well across the full multidrizzle mosaic. A proper measurement and continued monitoring of the wavelength-dependent GDC is scheduled for later in Cycle 17 and beyond.

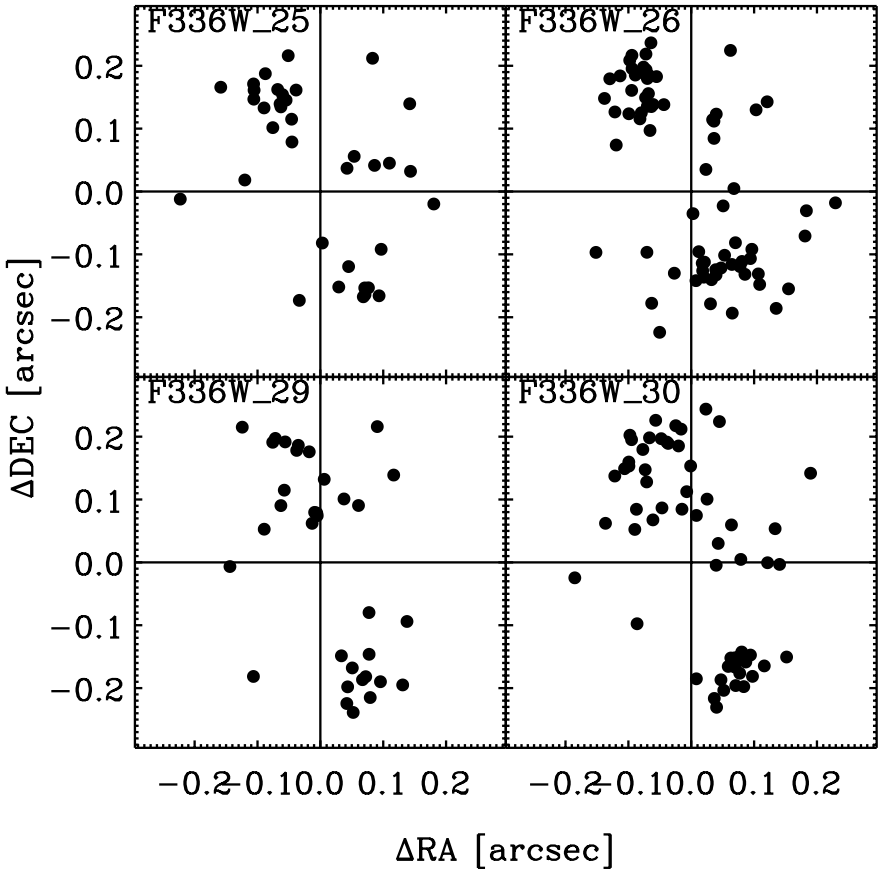

Fig. 4b. The astrometric residuals for four of our ERS pointings in the F336W filter (visits 25, 26, 29, 30). Note that *all four* visits show similar bimodal residuals, suggesting that this is a systematic error. We suspect that this is due to the wavelength-dependent geometrical distortion in the UV, since the only currently available distortion solution was measured in F606W. Since two distinct blobs of points occur in *similar locations in all four panels,* the multidrizzle images of objects seen in only one pointing — which includes 80–90% of the total ERS area (see Fig. 3 and 8a) — *are* round at 0.″090 pixel sampling. However, the images of the brighter objects in the overlap areas between mosaic pointings — 10–20% of the total area — are not always round, as can be seen in Fig. 4a.

Fig. 5a. Panchromatic 10-band color image of the entire ERS mosaic in the CDF-South. [This image is only displayed in the electronic version of this journal paper.] Shown is the common cross sections between the 4×2 ERS UVIS mosaics, the GOODS v2.0 ACS BViz, and the 5×2 ERS IR mosaics. The total image shown is 6500 × 3000 pixels, or 9.75 × 4.5 arcmin. We used color weighting of the 10 ERS filters as described in the text, and log(log) stretch. A higher resolution version of this image may be obtained from this URL[34].

[34] http://www.asu.edu/clas/hst/www/wfc3ers/ERS2_loglog.tif

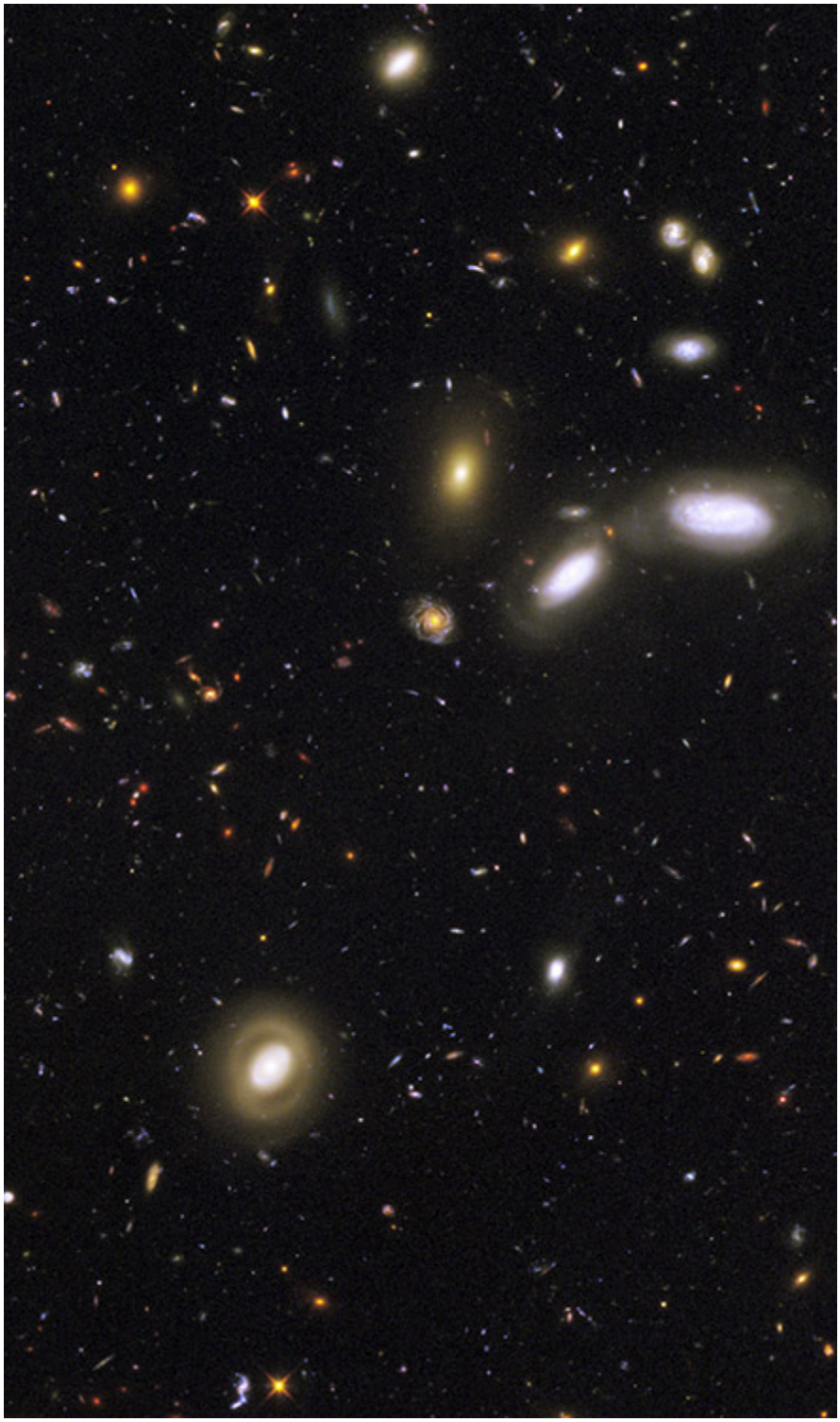

Fig. 5b. Zoom of the panchromatic 10-band ERS color image in the CDF-South (see Fig. 5a). The total image is 6500 × 3000 pixels, or 9.75 × 4.5 arcmin. A higher resolution version of this image may be obtained from this URL[35].

[35] http://www.asu.edu/clas/hst/www/wfc3ers/ERS2_gxysv4ln.tif

Fig. 6a. Color reproduction of a bright but unsaturated star image in the 10-band ERS color images in the CDF-South. Fig. 6b. Same for a double star. These images give a qualitative impression of the significant dynamic range in both intensity and wavelength that is present in these panchromatic ERS images.

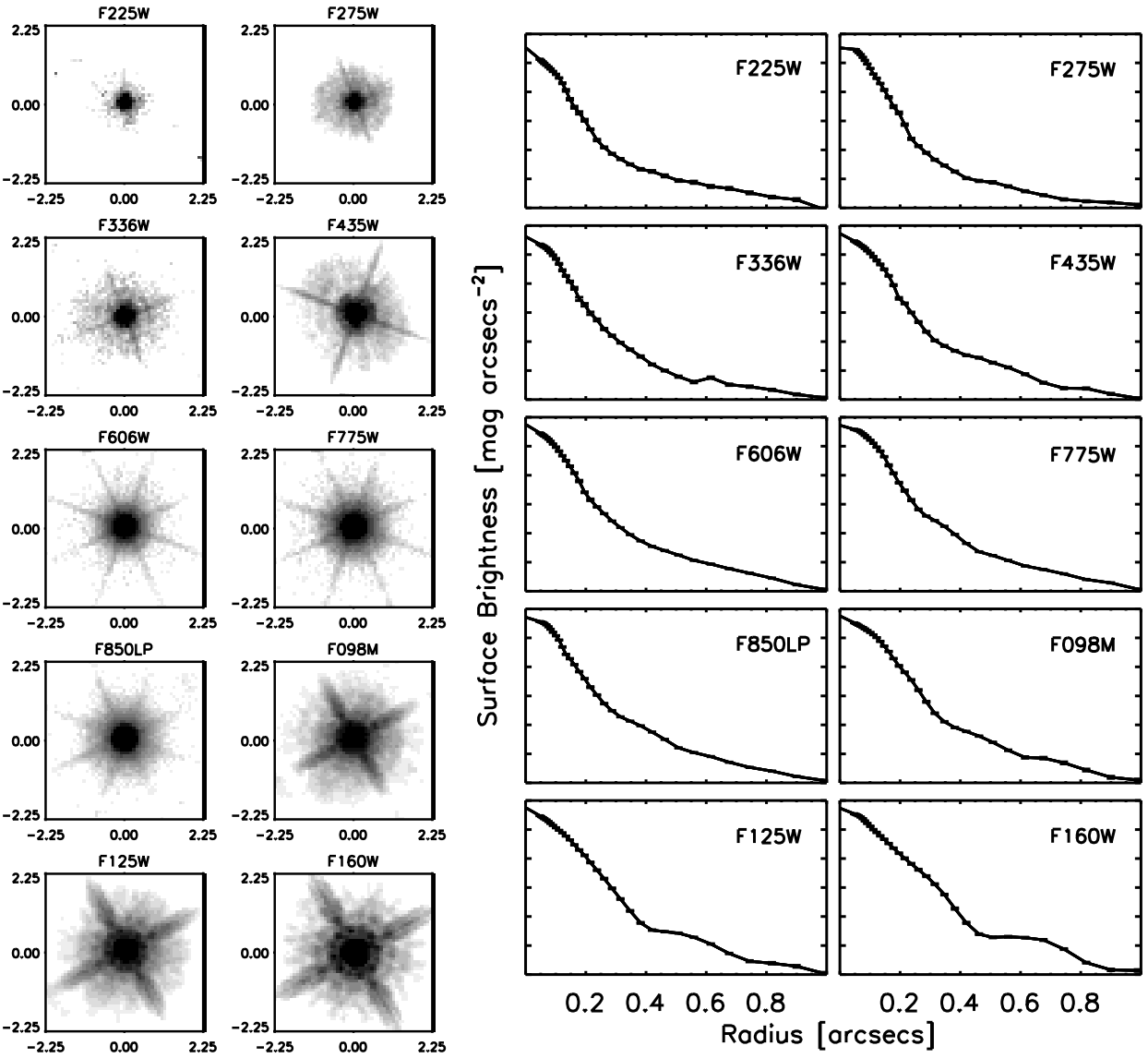

Fig. 7a (left panels). Stellar images, and Fig. 7b (right panels). stellar light-profiles in the panchromatic 10-band ERS color image in the CDF-South. Note the progression of λ/D, except that at wavelengths shorter than the V-band, HST is no longer diffraction limited, resulting in wider image-wings and a somewhat larger fraction of the stellar flux visible outside the PSF-core. The "red halo" at $\lambda \gtrsim 0.8$ μm is due to noticeable Airy rings in the stellar images in the WFC3 IR channel, and the red halo in the ACS z-band (Wong et al. 2010).

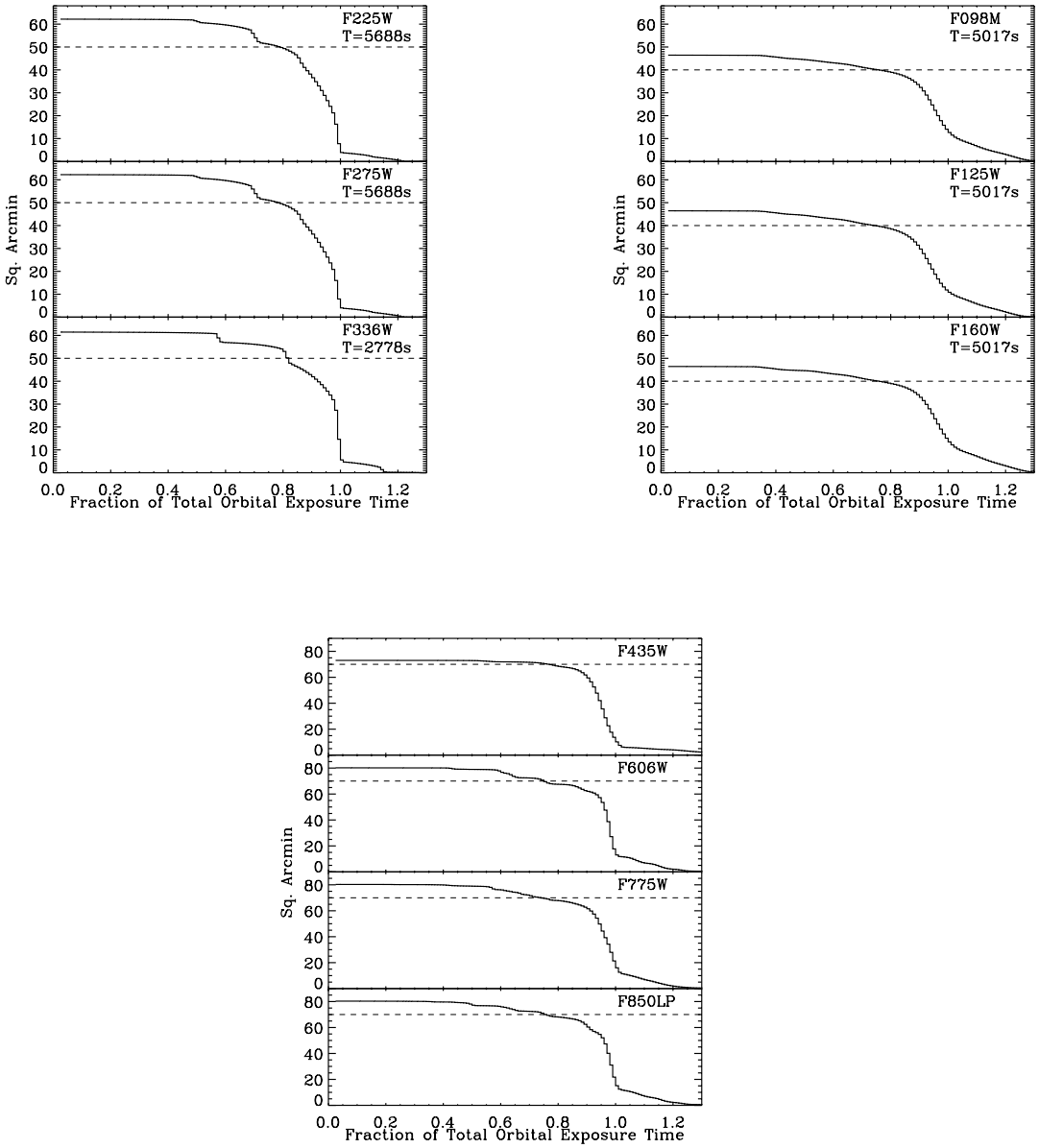

Fig. 8a (TOP LEFT panels). Cumulative distribution of the maximum pixel area that has the specified fraction of total orbital exposure time in each ERS filter. These effective areas must be quantified in order to properly do the object counts in Fig. 11a. About 50 arcmin^2 has ∼80% of the exposure time or ∼90% of the intended UV sensitivity. Fig. 8b (BOTTOM MIDDLE panels) Same as Fig. 8a, but for the GOODS v2.0 images in BViz. Fig. 8c (TOP RIGHT panels) Same as Fig. 8a, but for the ERS mosaics in the IR. About 40 arcmin^2 has ∼80% of the exposure time in the ERS IR mosaics, or ∼90% of the intended IR sensitivity. The overall WFC3 UVIS – IR sensitivity is 9–18% better than predicted from the ground-based thermal vacuum tests (see § 2 and Fig. 2), and so in essence 100% of the intended exposure time was achieved over the 50 arcmin^2 UVIS images and the 40 arcmin^2 IR images.

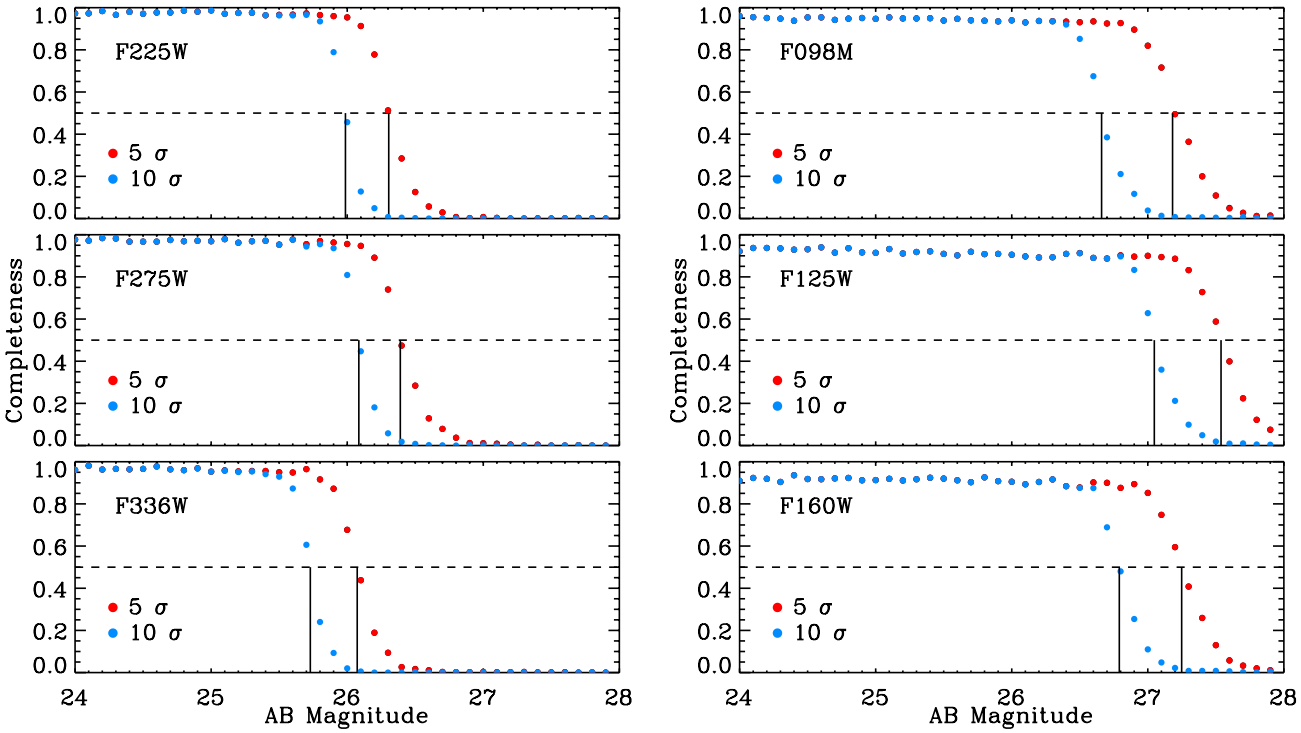

Fig. 9. Panchromatic completeness functions of the galaxy number counts in the ERS images. Violet, dark and light blue lines indicate WFC3/UVIS F225, F275, F336W; and orange through red lines indicates WFC3/IR F098M, F125W, and F160W, respectively. These were derived by Monte Carlo insertion of faint objects into the ERS images, and plotting the object recovery ratio as a function of total magnitude). The ACS BViz samples in the ERS area (not shown here) are substantially deeper, and are substantially complete to AB$\lesssim$28.5–27.5 mag, respectively (Table 1).

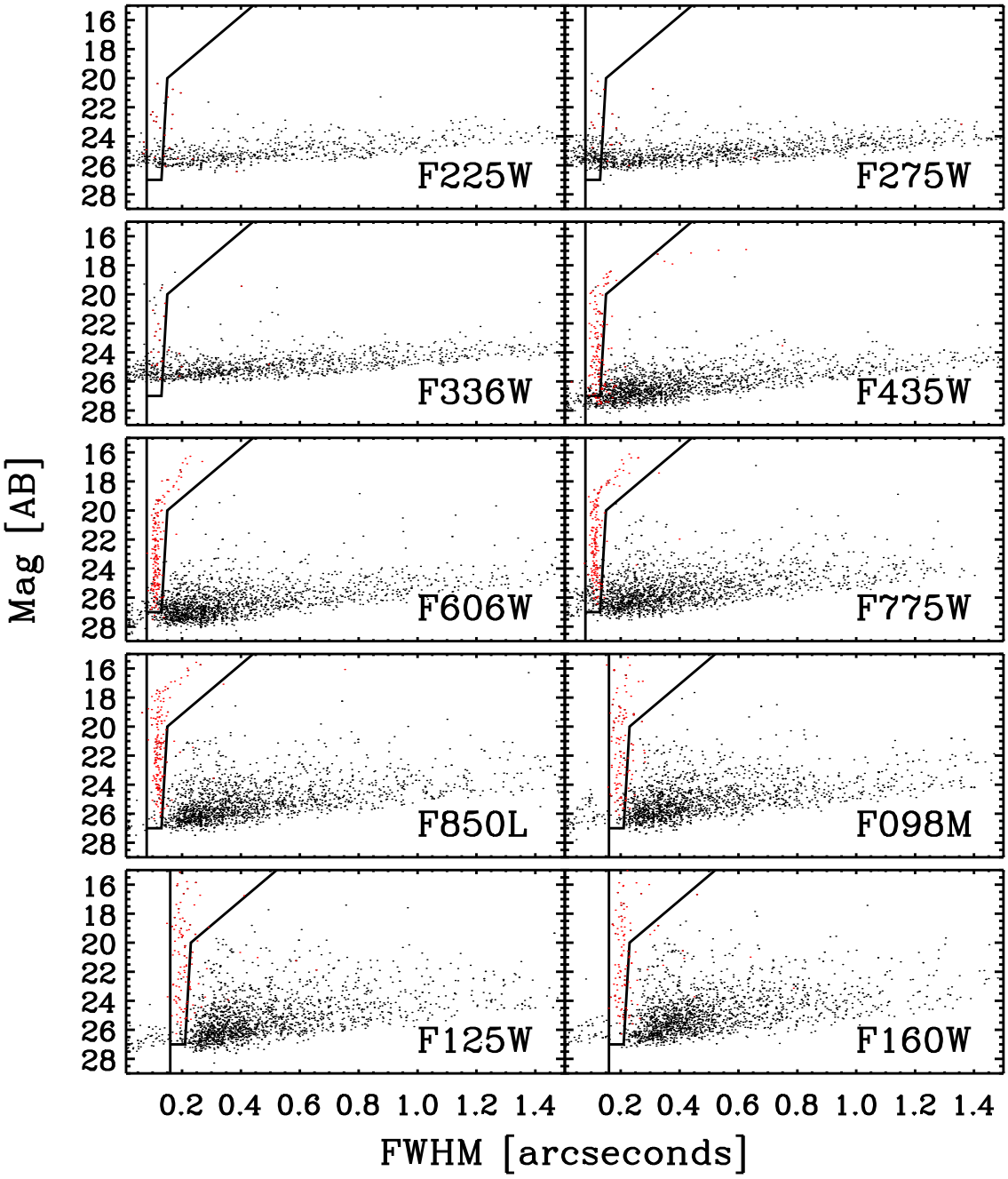

Fig. 10. Panchromatic star-galaxy separation in the 10-filter ERS images. Objects with $r_e \lesssim 0.9$ FWHM, where FWHM from Table 2 (or 0.″07–0.″15 FWHM) are image defects (plotted as black dots). Objects in the thin vertical filaments (plotted as red dots) immediately larger than this are stars. Objects to the right of the full-drawn slanted lines are galaxies (plotted as black dots). The star-galaxy separation breaks down at AB $\gtrsim$ 26–27 mag in UVBVizYJH, respectively. Details are discussed in the text. [A full resolution version of this figure is available on this URL[36].

[36] http://www.asu.edu/clas/hst/www/wfc3ers/ERS2_gxysv4ln.tif

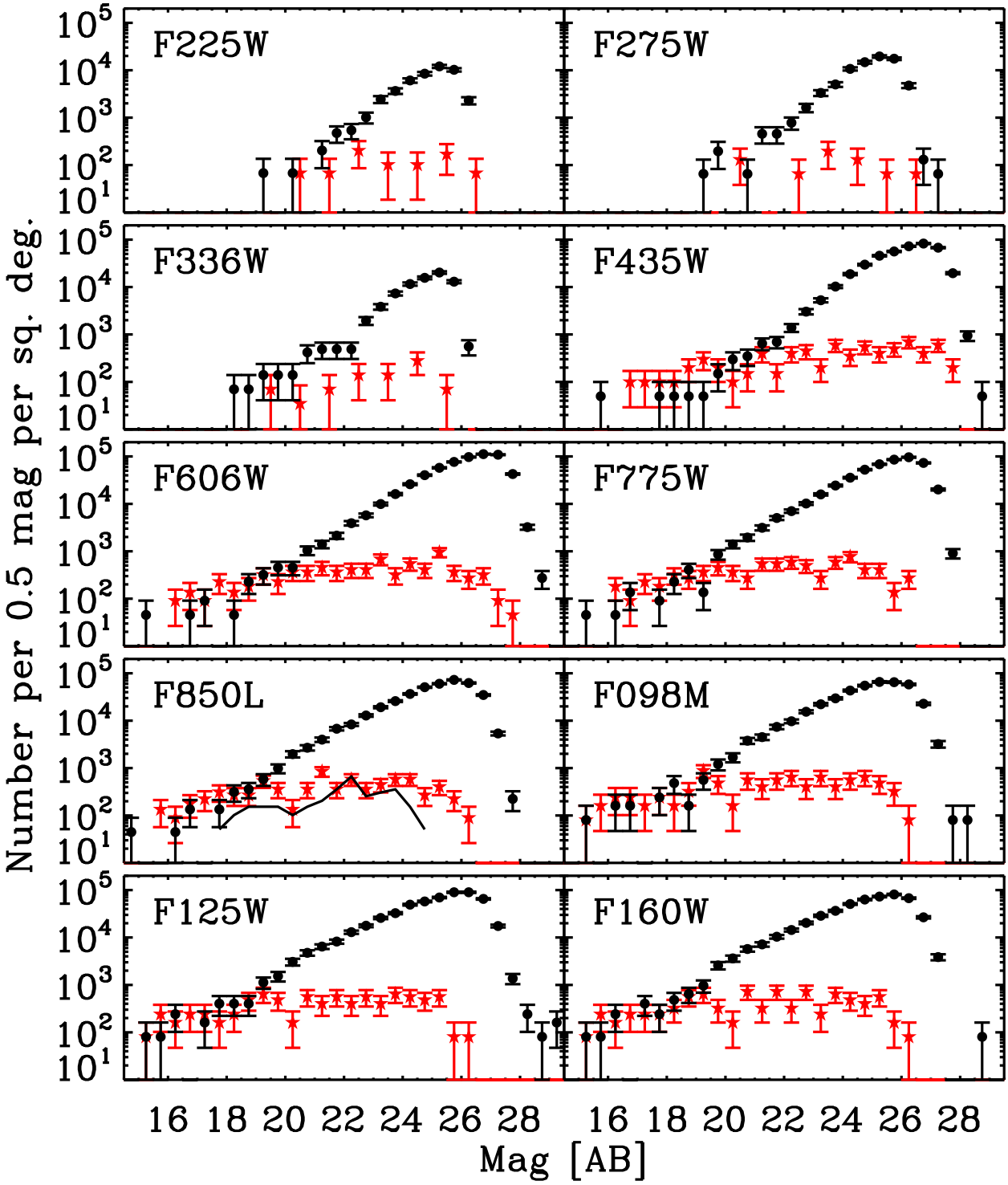

Fig. 11a. Panchromatic star counts (red asterisks) and panchromatic galaxy number counts in the ERS images (black dots), with the optimized star-galaxy separation from Fig. 10. All 10 ERS filters are shown in units of object numbers per 0.5 mag per deg^2, but in the three bluest filters (F225W, F275W, and F336W) the bins were doubled to 1.0 mag in width to improve statistics. The solid black line in the F850LP panel are the spectroscopic star counts from the HST GRAPES and PEARS ACS grism surveys of Pirzkal et al. (2005, 2009), which are in good agreement with our F850LP star counts.

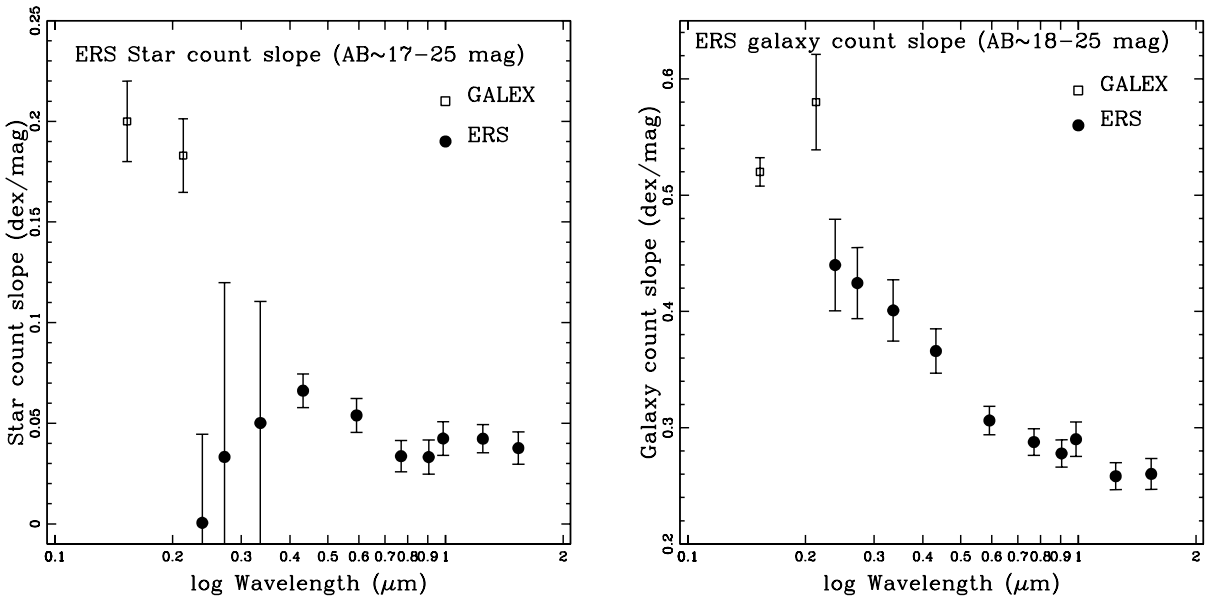

Fig. 11b. (LEFT) ERS Star count slope (filled circles) versus observed wavelength in the flux ranges AB≃19–25.5 mag for the 3 UV WFC3 filters, AB≃16–26 mag for the GOODS/ACS BViz filters, and AB≃15–25 mag for the 3 WFC3 IR filters, respectively. The faint-end of the Galactic star count slope is remarkably flat at all wavelengths from the mid–UV to the near-IR, with best fit power-law slopes in general of order 0.03–0.06 dex/mag. The two bluest points at 153 and 231 nm are from the GALEX star counts of Xu et al. (2005; open squares), which cover AB=17–23 mag.

11c. (RIGHT) ERS Galaxy count slope (filled circles)versus observed wavelength in the flux ranges AB≃19–25 mag for the 3 UV WFC3 filters, AB≃18–26 mag for the GOODS/ACS BViz filters, and AB≃17–25 mag for the 3 WFC3 IR filters, respectively. The two bluest points at 153 and 231 nm are from the GALEX galaxy counts of Xu et al. (2005; open squares), which cover AB=17–23 mag. The galaxy counts show the well known trend of a steepening of the best-fit power-law slope at the bluer wavelengths, which is caused by a combination of the more significant K-correction and the shape of the galaxy redshift distribution at the selection wavelength.

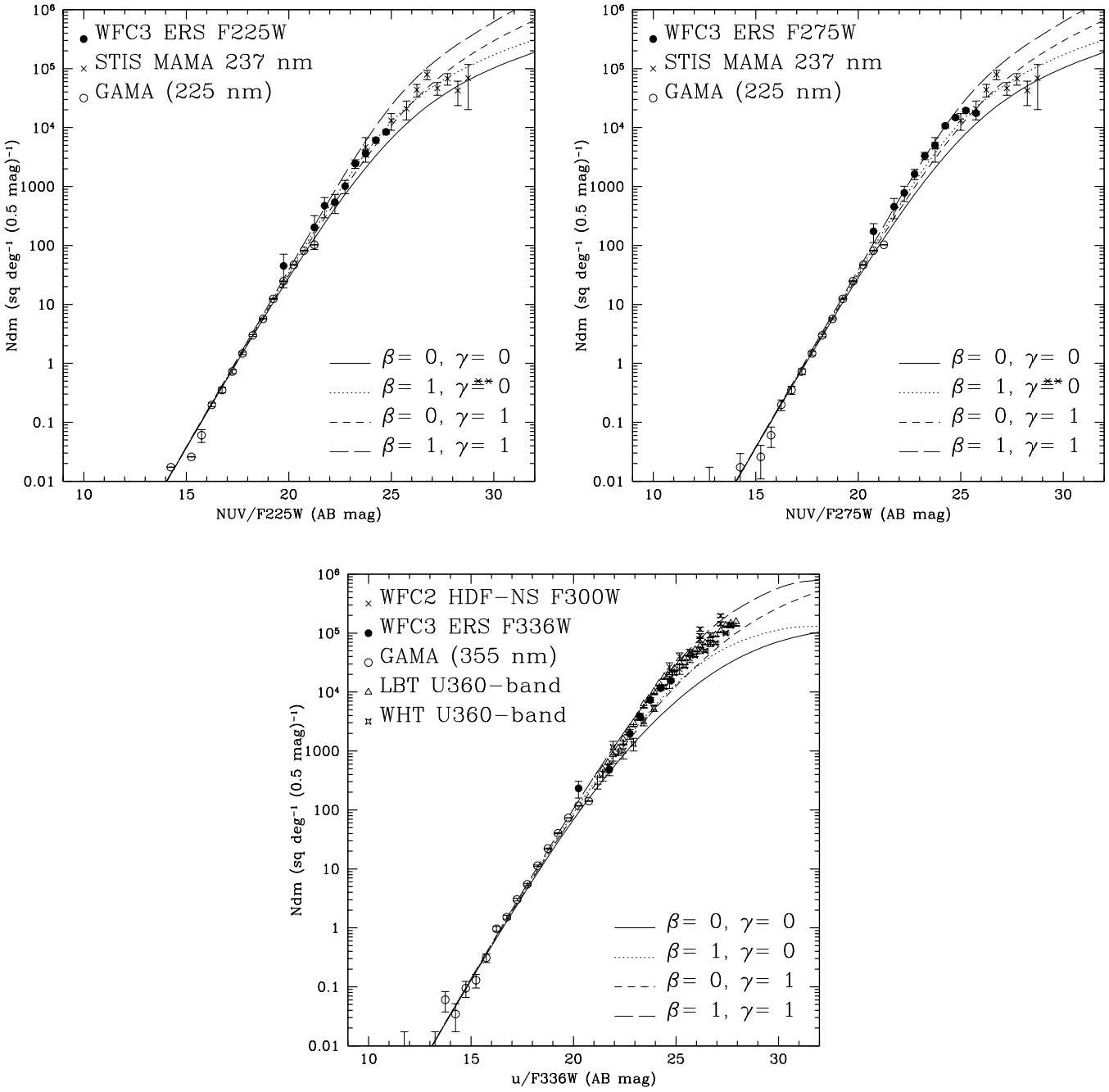

Fig. 12. Galaxy number counts for the entire flux range AB=10–30 mag in the F225W (12a), F275 (12b), and F336W (1c) filters. For comparison at the bright end, we added to the ERS number counts from Fig. 11 the panchromatic GAMA survey (Driver et al. 2009) counts in NUV+uvgriYJH, which cover AB=10–21 mag (Xu et al. 2005; Hill et al. 2010a). At the faint end, we added the WHT U-band and HDF-North and South F300W counts of Metcalfe et al. (2001), the deep LBT U-band counts of Grazian et al. (2009), as well as the deep HST STIS counts of Gardner et al. (2000). Best fit luminosity and number density evolution models range from AB=10–31 mag (see Driveret al. 1998; Hill et al. 2010a).

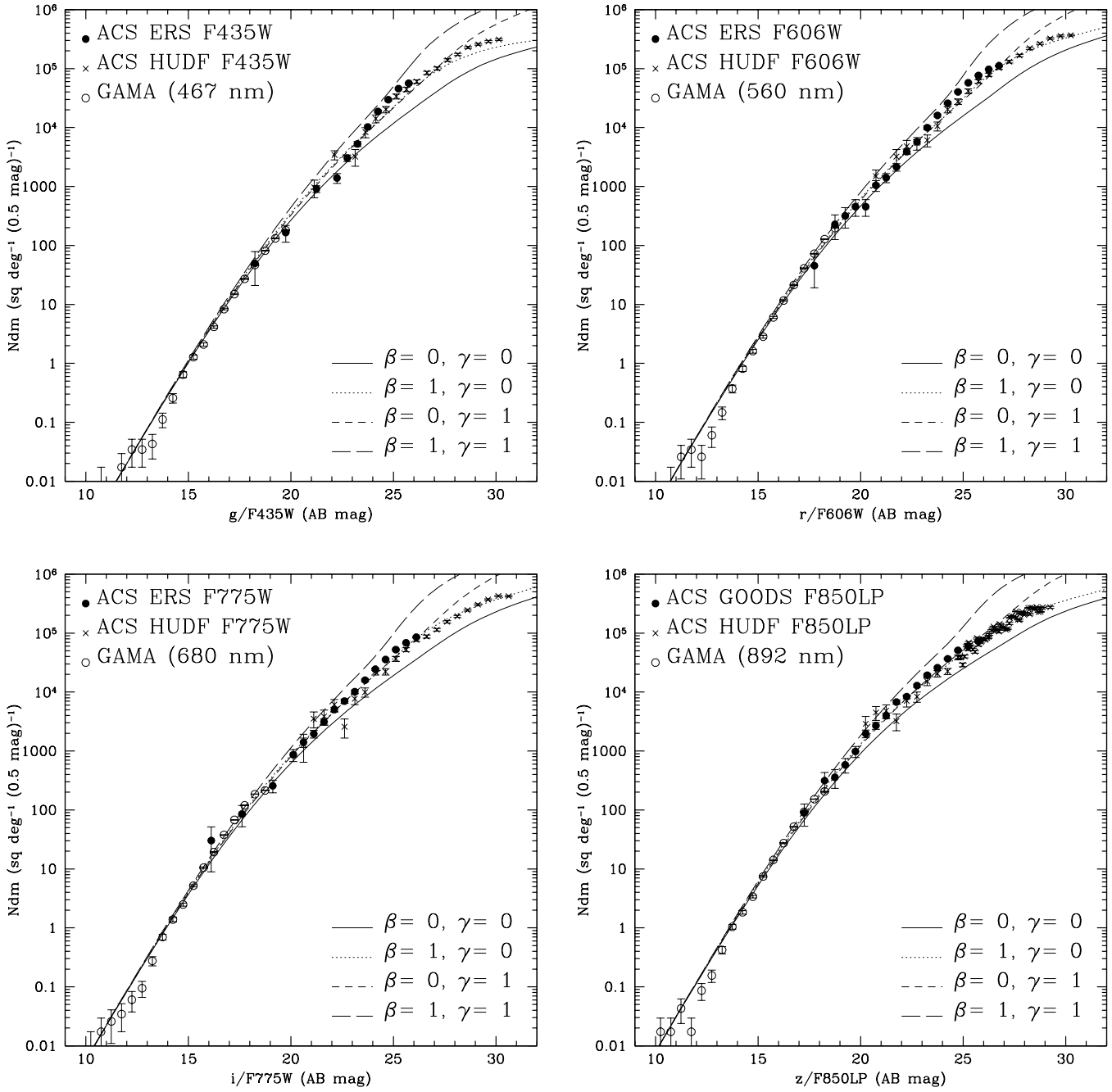

Fig. 12 (cont). Galaxy number counts for the entire flux range AB=10–30 mag in the F435W (12d), F606W (12e), F775W (12f), and F850LP (12g) filters. For comparison at the bright end, we added to the ERS number counts from Fig. 11 the panchromatic GAMA survey (Driver et al. 2009) counts in NUV+uvgriYJH, which cover AB=10–21 mag (Xu et al. 2005; Hill et al. 2010a). At the faint end, we added the HUDF counts in BViz from Beckwith et al. (2006), which cover AB=23–30 mag. Best fit luminosity and number density evolution models range from AB=10–31 mag (see Driveret al. 1998; Hill et al. 2010a).

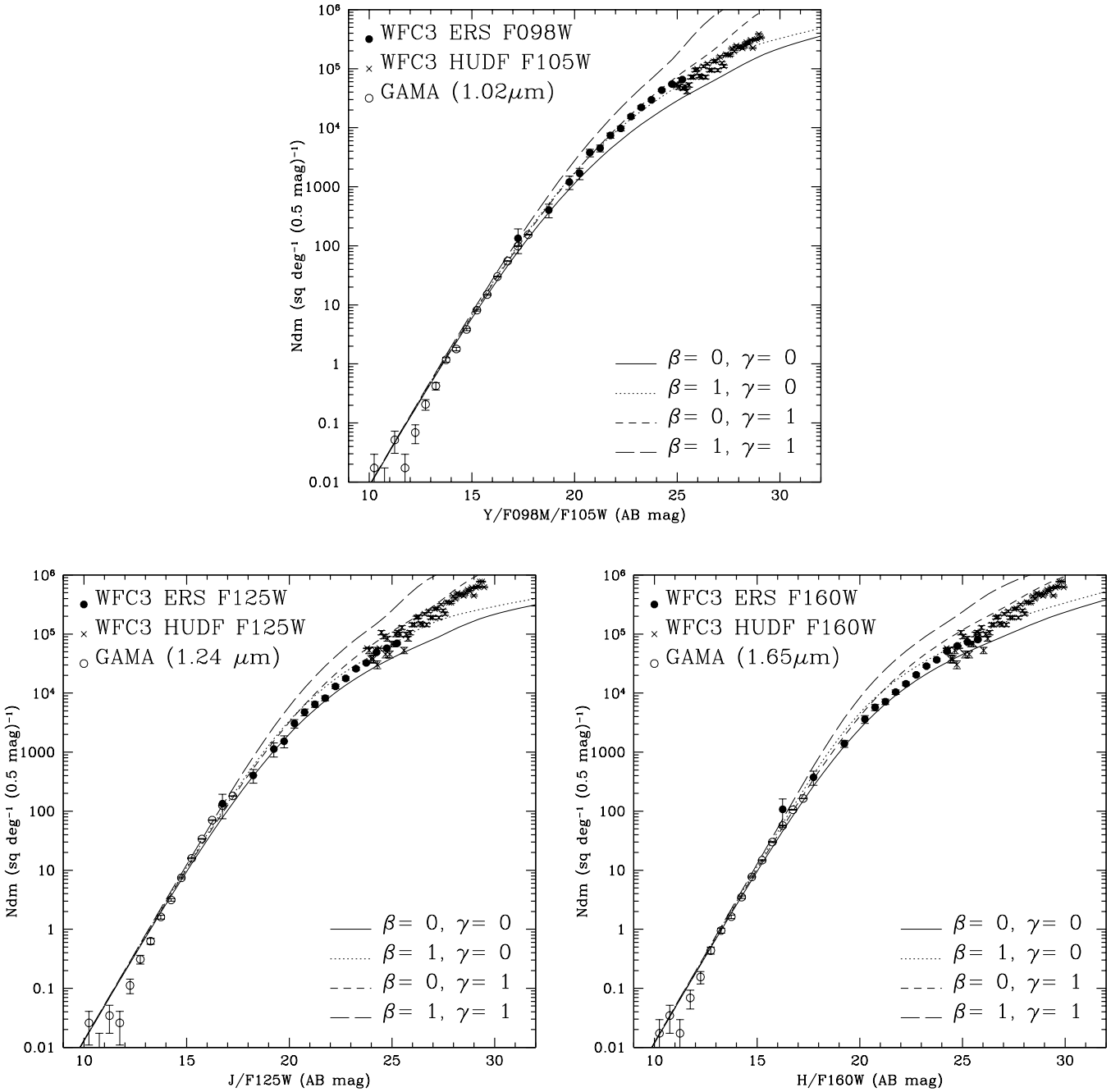

Fig. 12 (cont). Galaxy number counts for the entire flux range AB=10–30 mag in the F098M/F105W (12h), F125W (12i) and F160W (12j) filters. For comparison at the bright end, we added to the ERS number counts from Fig. 11 the panchromatic GAMA survey (Driver et al. 2009) counts in NUV+uvgriYJH, which cover AB=10–21 mag (Xu et al. 2005; Hill et al. 2010a). At the faint end, we added the HUDF counts in YJH from the Bouwens et al. (2009) YJH data as compiled by Yan et al. (2009), which cover AB=24–30 mag. In the UV, we added WHT U-band and HDF-North and South F300W counts of Metcalfe et al. (2001), the deep LBT U-band counts of Grazian et al. (2009), as well as the deep HST STIS counts of Gardner et al. (2000). Best fit luminosity and number density evolution models range from AB=10–31 mag (see Driveret al. 1998; Hill et al. 2010a).

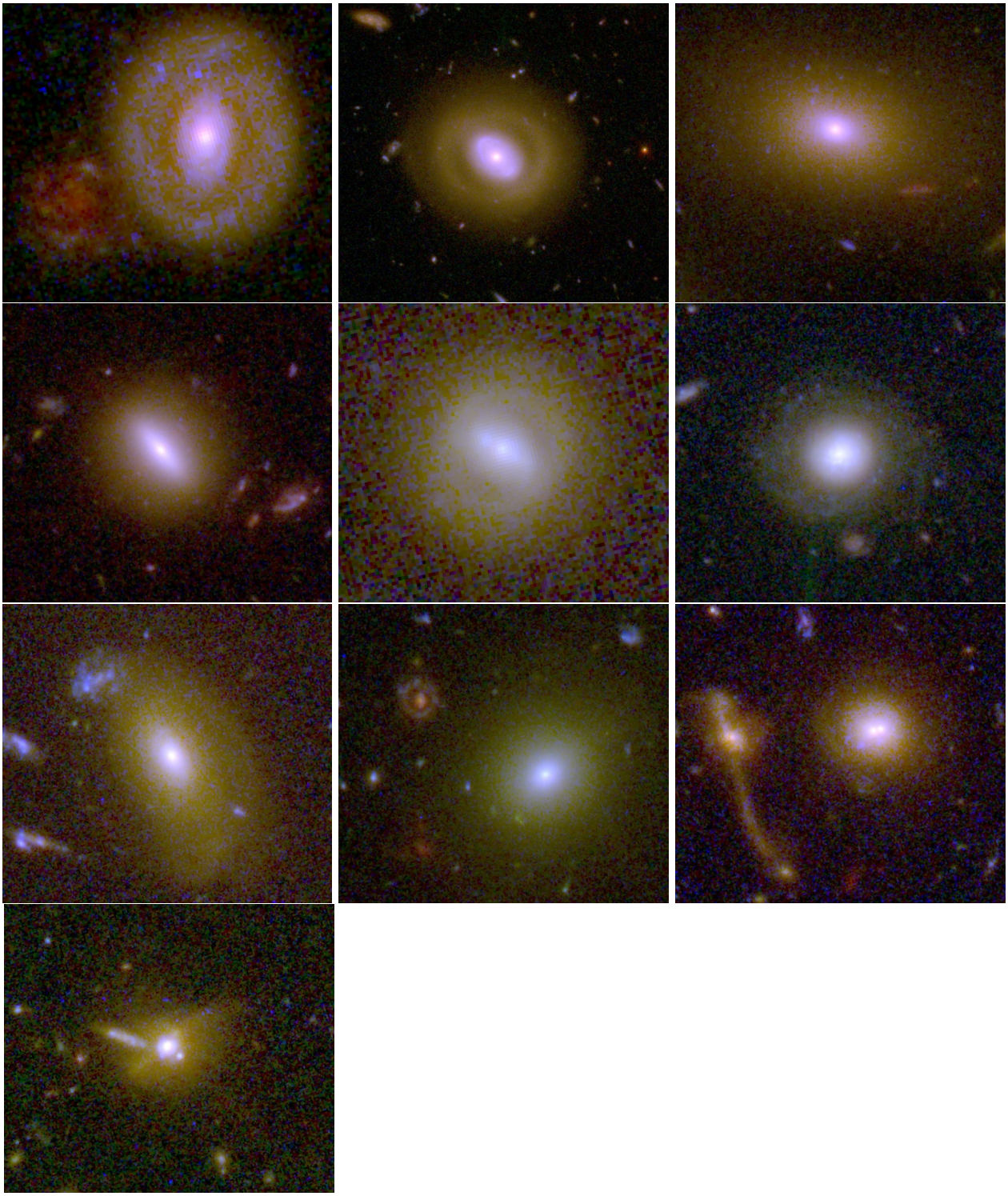

Fig. 13. Panchromatic postage stamps of early-type galaxies in the ERS with nuclear star-forming rings, bars, or other interesting nuclear structure. Each postage stamp is displayed at a slightly different color stretch that best brings out the UV nuclear structure.

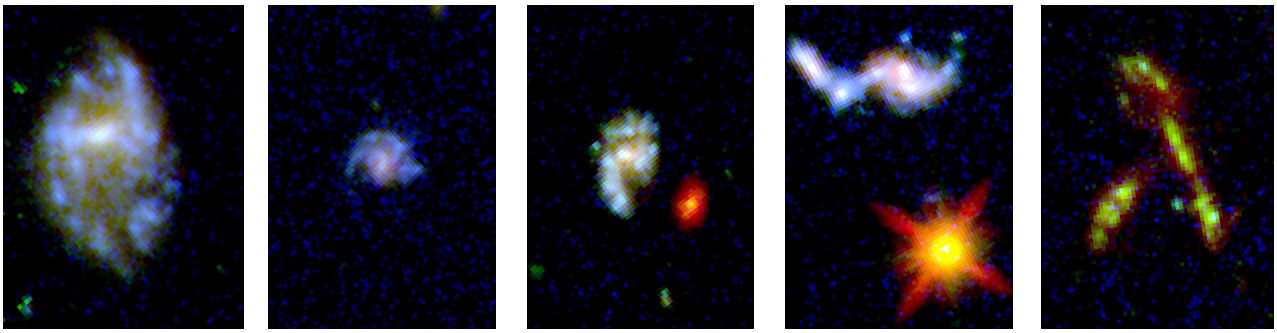

Fig. 14. Panchromatic postage stamps of objects with interesting morphological structure in the 10-band ERS color images of the CDF-S: from left to right, high signal-to-noise ratio detections of ERS galaxies resembling the main cosmological parameters H_0 , Ω, ρ_o, w, and Λ, respectively. These images illustrate the rich and unique morphological information available in the 10-band panchromatic ERS data set.